Large-Eddy Simulation of Decaying Stably Stratified Turbulence

DAVID A. SIEGEL

Department of Geography and Center for Remote Sensing and Environmental Optics, University of California at Santa Barbara, Santa Barbara, California

J. ANDRZEJ DOMARADZKI

Department of Aerospace Engineering, University of Southern California, Los Angeles, California

(Manuscript received 2 July 1990, in final form 15 March 1994)

ABSTRACT

A large-eddy simulation (LES) model is developed and employed to study the interactions among turbulent and internal gravity wave motions in a uniformly stratified fluid at oceanic space and time scales. The decay of a random initial energy spectrum is simulated in a triply periodic domain (L = 10 m) by solving the full nonlinear, three-dimensional Navier–Stokes equations using pseudospectral techniques and a numerical resolution of 64^3 modes. The subgrid scale (SGS) fluxes are parameterized using the Smagorinsky SGS flux parameterization. Three experiments were performed with mean buoyancy frequencies (N) of 1, 3, and 10 cph for a period of 10 buoyancy times (Nt).

The temporal evolution of the domain-averaged statistics is used to examine the nature of decaying stratified turbulence. Initially ($0 \leq Nt \leq 2$), energy levels rapidly decay as the spectral energy distributions evolve toward more isotropic forms. During this time, the buoyancy flux (BF) remains negative indicating a conversion of kinetic to potential energy and downgradient scalar mixing. After an initial period of decay ($Nt \geq 2$), rapid oscillatory exchanges of vertical kinetic energy (VKE) and potential energy (PE) are observed. These energy exchanges are driven by a nearly reversible BF that is supporting internal gravity wave motions. Synchronous oscillations in horizontal kinetic energy are also found although their amplitudes are significantly smaller. Irreversible aspects of the BF can still be observed during this latter stage of decay, especially for the N = 1 and 3 cph experiments. Estimates of the irreversible portion of BF are used to determine values of vertical eddy diffusivity, K_ρ, for this period. Resulting values for K_ρ are 2.4×10^{-5} and 7.2×10^{-5} m^2 s^{-1}, for the N = 1 and 3 cph experiments, respectively, consistent with oceanographic estimates for the main thermocline.

The domain-averaged energetics indicate that, although an equipartition is not observed between PE and the total kinetic energy, a robust equipartition is observed between the "wave" kinetic energy and PE. However, this equipartition does not appear to hold spectrally. Spectral analyses also indicate that the larger spatial scales are dominated by "vortical" energy. Evaluation of SGS energetics, fluxes, and dissipation rates indicates that SGS motions control energy dissipation rates but make small contributions to the energetics and fluxes, consistent with the LES assumptions. Spectral analyses of the SGS eddy viscosity and energy transfer rates are used to suggest improvements for future LES experiments of stably stratified turbulence.

One of the most exciting observations made here is the rapid transition in the character of the buoyancy flux evolution as part of the "turbulent collapse." The BF changes suddenly from a state of irreversible mixing to an oscillatory, nearly reversible BF when the Ozmidov length scale is the same order as the vertical energy-containing length scale [i.e., the Froude number becomes O(1)]. Vertical temperature cross sections also exhibit some evidence of the collapse (i.e., chaotic structures evolving into wavelike variations). However, these changes occur gradually compared with the rapid transition observed in BF. Unlike most previous laboratory observations, energy decay rates and characteristic length scales appear to be unaffected by this dynamic transition. It is speculated that differences between the present LES results and previous laboratory and numerical results may be attributed to extreme differences in the Reynolds numbers for these flows.

1. Introduction and motivations

The kinematics and dynamics of small-scale (1 cm to 100 m) thermocline motions have been intensively observed and modeled for more than 20 years (e.g., Garrett and Munk 1972, 1975; Osborn and Cox 1972; Gregg 1977, 1989, 1991; Müller et al. 1978, 1986; Osborn 1980; Gibson 1980, 1987; Munk 1981; Gargett et al. 1981, 1984; Dillon 1982, 1984; Pinkel 1984; Gargett 1984; Gregg et al. 1986, 1993; Crawford 1986; Gregg and Stanford 1988; Kunze et al. 1990; Moum 1990; Pinkel et al. 1991). However, much remains unclear concerning the role of these motions in the vertical transports of heat and momentum in the oceanic interior (e.g., Munk 1981; Holloway 1983, 1988; Gregg 1987, 1989). Knowing the role of these small-scale dy-

Corresponding author address: Dr. David A. Siegel, Dept. of Geography, 3611 Ellison Hall, University of California at Santa Barbara, Santa Barbara, CA 93106.

© 1994 American Meteorological Society

namical processes is important for a variety of purposes, including: the parameterization of mixing processes for large-scale oceanographic general circulation models, the interpretation of 1D microstructure observations, and the evaluation of the effects of turbulence and small-scale advection on oceanic biogeochemical processes. Unfortunately, it appears unlikely that in situ, 3D observations of small-scale thermocline motions will be obtained in the near future. Hence, the 3D numerical simulation of small-scale oceanic motions, made at the proper time and space scales, may be the only expedient means of investigating these motions.

Previous numerical investigations of ocean turbulence have generally been made using either a two-dimensional (vertical–horizontal) geometry (e.g., Orlanski and Cerasoli 1981; Weissman et al. 1981; Shen and Holloway 1986; Henyey et al. 1986; Holloway and Ramsden 1988; Winters and D'Asaro 1989; Ramsden and Holloway 1991) or in 3D at low Reynolds numbers (e.g., Riley et al. 1981; Holloway and Ramsden 1988; Métais and Herring 1989; Ramsden and Holloway 1991; Winters and Riley 1992). Both of these assumptions place severe restrictions on the resulting numerically simulated flows. For example, the 2D assumption restricts the characteristic types of motions that can be simulated as well as the number and types of possible nonlinear interactions (e.g., Müller et al. 1986; Lesieur 1987; Müller 1988; Lelong and Riley 1992). Further, direct 3D numerical simulations must be made at low Reynolds number due to finite computational resources. This means that molecular viscous and diffusive processes will play an inordinately important role in the evolution of the energy-containing scales. For ocean thermocline motions, typical Reynolds numbers are quite large ($\mathrm{Re} = UL/\nu \sim 5 \times 10^5$ for $L = 10$ m, $U = 0.05$ m s^{-1}, and $\nu = 10^{-6}$ m^2 s^{-1}). Thus, molecular processes occur at scales many orders of magnitude smaller than the energy-containing scales (e.g., Tennekes and Lumley 1972; Gregg 1987; Moum 1990). These facts indicate that *direct* numerical methods cannot realistically simulate the 3D motions of oceanic turbulence and numerical simulations must be made at the appropriate temporal and spatial scales.

Here, we numerically simulate the decay of stably stratified turbulence at oceanographically relevant time- and space scales using the large-eddy simulation (LES) method. Although it is unlikely that a decaying simulation will realistically depict the small-scale, quasi-steady ocean, these results still provide many insights into the dynamics and kinematics of ocean turbulence under the influence of stable stratification. Moreover, there are many oceanic flows, such as in a stratified tidal channel (e.g., Gargett et al. 1984) or in the evolution of a single overturning event (e.g., Hebert et al. 1992), where detailed knowledge of the decay processes of an initially turbulent region are of direct relevance.

Our study is one of the first applications of LES techniques to oceanographic flows and, in some sense, provides the building blocks upon which more complex LES oceanic models may be based. Large-eddy simulations have been used extensively in the atmospheric sciences to study the evolution of the planetary boundary layer (e.g., Deardorff 1973, 1980; Moeng 1984; Moeng and Wyngaard 1988; Schmidt and Schumann 1989; Mason 1989; Ebert et al. 1989; Mason and Derbyshire 1990). However, these techniques have only recently been applied to oceanographic problems (e.g., Siegel 1988, 1991; Gallacher 1990; McWilliams et al. 1993).

In the present paper, the construction and implementation of a large-eddy simulation model of the decay of stably stratified turbulence at oceanic time and space scales is described. In the next section, the initial value problem for decaying turbulence under the influence of stable stratification is formulated. The third section introduces the large-eddy simulation method and illustrates how subgrid-scale (SGS) processes are differentiated mathematically from grid-scale (GS) motions. Next, the details of the derivation of the Smagorinsky SGS flux model are presented along with its modification due to the influence of buoyancy forces. The fifth section describes the initialization procedure followed by a brief description of the pseudospectral numerical procedure that is employed. The results section depicts the time evolution of flow energetics as the dynamical role of buoyancy processes become dominant. In particular, the role of the buoyancy flux is examined in detail as is the partitioning of the kinetic energy into "wave" and "vortical" components. Section 8 illustrates several of the visual aspects of the flow field, and in section 9 the spectral structure of the flow field and energy transfer rates is explored. The discussion sections assess the performance of the SGS parameterization as well as addressing several aspects of the transition from a fully turbulent flow to one where buoyancy processes become dominant, the so-called turbulent collapse. The reader familiar with the large-eddy simulation method may wish to skip directly from the description of the initial-value problem (section 2) to the formulation of initial conditions (section 5).

2. Problem statement

The decay of a specified initial energy distribution in a linearly stratified fluid is numerically simulated by solving the 3D, nonrotating Navier–Stokes equations under the assumptions that the fluid is incompressible, the Boussinesq approximation is satisfied, and that temperature is the single stratifying agent. Under these assumptions, the equations of motion may be written as

$$\frac{\partial u_i}{\partial t} = -\frac{\partial u_i u_j}{\partial x_j} - \frac{\partial p}{\partial x_i} + \alpha g \delta_{i3} T + \nu \frac{\partial^2 u_i}{\partial x_j \partial x_j} \quad (1a)$$

$$\frac{\partial T}{\partial t} = -\frac{\partial u_j T}{\partial x_j} - u_3 \frac{dT_s}{dx_3} + \kappa \frac{\partial^2 T}{\partial x_j \partial x_j} \quad (1b)$$

$$\frac{\partial u_i}{\partial x_i} = 0, \quad (1c)$$

where t is time, $\mathbf{x}_i$ is the spatial vector ($\mathbf{x}$; x_i; x_1, x_2, x_3; x, y, z), $\mathbf{u}_i$ is the velocity vector ($\mathbf{u}$; u_i; u_1, u_2, u_3; u, v, w), p is the pressure perturbation from the hydrostatic balance (normalized by the mean density), T is the perturbation temperature from the horizontal mean temperature ($T_s(x_3)$, which describes the stable background profile), g is the magnitude of gravitational acceleration (9.8 m s^{-2}); α is the coefficient of thermal expansion (0.025 K^{-1}), ν is the kinematic viscosity (10^{-6} m^2 s^{-1}); κ is the thermal diffusivity (10^{-6} m^2 s^{-1}); δ_{i3} is the Kronecker-delta function; and the summation convention is employed. The degree of stable stratification may be characterized by the buoyancy frequency, N, which is given by

$$N = \left(\alpha g \delta_{i3} \frac{dT_s}{dx_i} \right)^{1/2}, \quad (2)$$

where N provides an upper bound to the frequency range of linear internal waves. The buoyancy frequency is constant, corresponding to 1, 3, and 10 cph, and the equations of motion are integrated for 10 buoyancy times (Nt). The details of the initial conditions for u_i and T are presented in section 5.

The modeling domain is a triply periodic cube with sides of length, L. The boundary conditions may therefore be represented as

$$u_i(x_j) = u_i(x_j + nL), \quad (3a)$$

$$T(x_j) = T(x_j + nL), \quad (3b)$$

where n may be any integer. This allows spectral numerical techniques to be applied for efficiently evaluating the spatial derivatives using Fourier series (Orszag 1971a). Periodic boundary conditions are appropriate for the numerical simulation of homogeneous flows (Lesieur 1987).

The equations are nondimensionalized using the box size, $L/2\pi$, as the length scale, the buoyancy period, N^{-1}, as the timescale, and α^{-1} as the temperature scale. The factor of 2π in the definition of the length scale enables spatial wavenumbers to be defined as integer values. Hereafter, the nondimensionalized form of the equations of motion are utilized.

It should be noted that planetary vorticity is not considered in the present model, although Coriolis forces definitely have an important role in the evolution of ocean turbulence and its interactions with the internal wave field (e.g., Munk 1981; Gregg et al. 1986; Kunze et al. 1990). This allows us to restrict the number of independent timescales in the problem to a buoyancy time (N^{-1}) and an overturning time (L/U), whose ratio gives rise to a Froude number [Fr $\equiv U/(LN)$; see section 10b]. The inclusion of planetary vorticity would add another timescale (f^{-1}, where f is the Coriolis parameter) and another nondimensional group, the Rossby number. Similarly, the inclusion of a mean vertical shear adds yet another characteristic timescale [$(dU/dz)^{-1}$]. These additional complicating processes are ignored here in order to tightly constrain the problems investigated. We plan to investigate these effects in the near future.

To *directly* solve the above initial value problem, one must resolve not only the energy-containing scales of the flow, but also those scales where energy is dissipated by molecular processes. With finite computational resources, the spatial scales that may be numerically simulated *directly* are limited by the requirement that both the dissipation and energy-containing scales must be resolved. For example, typical oceanic values for the Kolmogorov length scale, the scale at which molecular viscosity becomes important (26a), range from 10^{-3} to 10^{-2} m. Present day computational standards restrict the number of wave modes that may be simulated to be O(100) in each direction. This means that for the *direct* simulation of ocean turbulence, the largest spatial domains that will be numerically resolved to something less than 1 m. This is far too small to contain any of the energy characteristic of ocean turbulence and the directly simulated Reynolds numbers will be much smaller (<100) than typical oceanographic values [O(10^5)]. To alleviate these difficulties, we apply the large-eddy simulation method.

3. The large-eddy simulation method

In a large-eddy simulation (LES), the three-dimensional Navier–Stokes equations are solved directly for the resolved scales of motion (or grid scale), while the effects of the unresolved scales (or subgrid scale) are parameterized in terms of the GS motions. This modeling of SGS processes allows oceanographically relevant Reynolds numbers to be simulated in a numerically achievable wave space. For example, Reynolds numbers (based upon Taylor length scales, Re_λ) for laboratory experiments or *direct* numerical simulations are typically less than 100, whereas oceanographic estimates are three orders of magnitude larger [O(10^5); Siegel 1991]. LES techniques enable high Reynolds number flows, such as ocean turbulence, to be numerically simulated using the correct balance of terms in the equations of motion.

In an LES, the wavenumber cutoff between GS and SGS motions is made within the inertial subrange of turbulence. This is done for two reasons. First, inertial subrange motions may be assumed to be locally isotropic (e.g., Tennekes and Lumley 1972). Second, the rate at which KE and PE are transferred across the

SGS cutoff must be equal to the rate at which they are dissipated by molecular processes (the KE dissipation rate, ϵ, and the PE dissipation rate, ϵ_P). These two facts greatly simplify the parameterization of the SGS motions. The large-eddy simulation approach is similar in spirit to the parameterization of small-scale motions in an eddy-resolving ocean general circulation model (OGCM; e.g., Holland and Lin 1975). However, it seems considerably simpler to parameterize SGS processes for the inertial subrange of turbulence than for the submesoscale turbulent motions required by an eddy-resolving OGCM (e.g., Onken 1992).

As discussed previously, defining the extent of the physical domain is problematic given a finite numerical resolution (or finite number of spatial modes). It involves the trade-off between being large enough to simulate oceanographically relevant motions, while remaining small enough for a portion of the inertial subrange to be resolved. The validity of the SGS parameterization is, in part, based upon the GS cutoff wavenumber ($k_c = \pi/\Delta$) lying within the inertial subrange of turbulence. The GS cutoff (Δ) depends upon the physical dimension of the box (L) and the numerical mesh resolution (M), or $\Delta = L/M$. For the present simulations, L ($=L_x = L_y = L_z$) is set equal to 10 m and M ($=M_x = M_y = M_z$) is 64. Thus, the simulated grid scales range from 0.156 to 10 m where the GS cutoff ($\Delta = 0.156$ m) corresponds well to observed ranges for the inertial subrange (e.g., Phillips 1980; Gargett et al. 1981, 1984).

In developing an LES model, the equations of motion are volume averaged to formally define the grid scale (GS) motions distinct from the subgrid scale (SGS). This scale separation is performed for any fluid variable $[f(\mathbf{x}; t)]$ by partitioning it into a GS $[\bar{f}(\mathbf{x}; t)]$ and an SGS $[f'(\mathbf{x}; t)]$ component (Leonard 1974), or

$$f(\mathbf{x}; t) = \bar{f}(\mathbf{x}; t) + f'(\mathbf{x}; t). \tag{4}$$

The GS value of a variable $[f(\mathbf{x}; t)]$ is evaluated as the convolution of $f(\mathbf{x}; t)$ with a prescribed spatial filtering function $[G(\mathbf{x})]$ or

$$\bar{f}(\mathbf{x}; t) = \int_D G(\mathbf{x} - \mathbf{x}') f(\mathbf{x}'; t) d\mathbf{x}', \tag{5}$$

where the integration is taken over the entire domain, D. In this work, a boxcar average in physical space is used as the filtering function,

$$G(\mathbf{x}) = \begin{cases} 1, & |\mathbf{x}| < \Delta \\ 0, & |\mathbf{x}| > \Delta, \end{cases} \tag{6}$$

where Δ is the physical space grid scale. This averaging procedure is implicit in the pioneering large-eddy simulations of Deardorff (1970) and Schumann (1975). Other filtering functions such as a spectral sharp-cut filter or a Gaussian weighted filter may be used. However, the advantages of these procedures do not appear to outweigh the cost, complexity and possible ambiguities in the interpretation of the resulting simulations, particularly for homogeneous flows (e.g., Kwak 1975; Clark et al. 1979; Mansour et al. 1979; Ferziger 1983; Eidson 1985; Lesieur 1987; Moeng and Wyngaard 1988). Application of the spatial averaging procedure (5) to the nondimensionalized equations of motion gives

$$\frac{\partial \bar{u}_i}{\partial t} = -\frac{\partial \overline{u_i u_j}}{\partial x_j} - \frac{\partial \bar{p}}{\partial x_i} + g\delta_{i3}\bar{T} + \nu \frac{\partial^2 \bar{u}_i}{\partial x_j \partial x_j} \tag{7a}$$

$$\frac{\partial \bar{T}}{\partial t} = -\frac{\partial \overline{u_j T}}{\partial x_j} - \bar{u}_3 \frac{dT_s}{dx_3} + \kappa \frac{\partial^2 \bar{T}}{\partial x_j \partial x_j} \tag{7b}$$

$$\frac{\partial \bar{u}_i}{\partial x_i} = 0. \tag{7c}$$

The nonlinear flux terms are also partitioned into GS and SGS components:

$$\overline{u_i u_j} = \overline{\bar{u}_i \bar{u}_j} + \overline{u_i' \bar{u}_j} + \overline{\bar{u}_i u_j'} + \overline{u_i' u_j'} = \bar{u}_i \bar{u}_j + \Lambda_{ij} - \tau_{ij} \tag{8a}$$

$$\overline{u_i T} = \overline{\bar{u}_i \bar{T}} + \overline{u_i' \bar{T}} + \overline{\bar{u}_i T'} + \overline{u_i' T'} = \bar{u}_i \bar{T} + \Lambda_{\theta i} - \tau_{\theta i}, \tag{8b}$$

where Λ_{ij} is the Leonard momentum flux $(\overline{\bar{u}_i \bar{u}_j} - \bar{u}_i \bar{u}_j)$, $\Lambda_{\theta i}$ is the Leonard heat flux $(\overline{\bar{u}_i \bar{T}} - \bar{u}_i \bar{T})$, τ_{ij} is the SGS momentum flux $(\overline{u_i' u_j'} + \overline{u_i' \bar{u}_j} + \overline{\bar{u}_i u_j'})$, and $\tau_{\theta i}$ is the SGS heat flux $(\overline{u_i' T'} + \overline{u_i' \bar{T}} + \overline{\bar{u}_i T'})$. The Leonard fluxes, a consequence of the nested averaging procedure (Leonard 1974), are negligible when boxcar averaging in physical space is applied (Clark et al. 1979; Yoshizawa 1982; Ferziger 1983; Eidson 1985; Siegel 1988). Applying the above definitions of the SGS fluxes and writing the GS nonlinear terms in the momentum equations in vorticity form, the GS equations of motion are equal to

$$\frac{\partial \bar{u}_i}{\partial t} = \epsilon_{ijk} \bar{u}_j \bar{\Omega}_k - \frac{\partial \bar{p}}{\partial x_i} - \frac{\partial (\bar{u}_j \bar{u}_j)/2}{\partial x_i} + g\delta_{i3}\bar{T} + \nu \frac{\partial^2 \bar{u}_i}{\partial x_j \partial x_j} - \frac{\partial \tau_{ij}}{\partial x_j} \tag{9a}$$

$$\frac{\partial \bar{T}}{\partial t} = -\frac{\partial \bar{u}_j \bar{T}}{\partial x_j} - \bar{u}_3 \frac{dT_s}{dx_3} + \kappa \frac{\partial^2 \bar{T}}{\partial x_j \partial x_j} - \frac{\partial \tau_{\theta j}}{\partial x_j} \tag{9b}$$

$$\frac{\partial \bar{u}_i}{\partial x_i} = 0, \tag{9c}$$

where the resolved scale vorticity vector, $\bar{\Omega}_i$, is defined using

$$\bar{\Omega}_i = \epsilon_{ijk} \frac{\partial \bar{u}_k}{\partial x_j} \tag{10}$$

and ϵ_{ijk} is the alternating tensor.

4. Parameterization of the SGS fluxes

To solve the resolved scale equations of motion (9), the SGS fluxes must be parameterized in terms of GS flow quantities. This is done usually by representing the SGS fluxes in flux-gradient form, or

$$\tau_{ij} = -K_{SGS}\bar{S}_{ij} + \frac{\tau_{kk}}{3}\delta_{ij} \tag{11a}$$

$$\tau_{\theta i} = -\frac{K_{SGS}}{Pr_t}\frac{\partial \bar{T}}{\partial x_i}, \tag{11b}$$

where $\bar{S}_{ij}$ is the GS rate of strain tensor ($=\partial\bar{u}_i/\partial x_j + \partial\bar{u}_j/\partial x_i$), K_{SGS} is the SGS eddy viscosity (still a function of $\mathbf{x}$ and t), and Pr_t is the SGS turbulent Prandtl number, which is defined as the ratio of the SGS eddy viscosity to the SGS eddy diffusivity. Subsequently, Pr_t will be assumed to be independent of both time and space, following previous LES investigations (e.g., Ferziger 1983; Eidson 1985; Lesieur 1987; Siegel 1991; Batchelor et al. 1992). The equations of motion with the modeled SGS fluxes are

$$\frac{\partial \bar{u}_i}{\partial t} = \epsilon_{ijk}\bar{u}_j\bar{\Omega}_k - \frac{\partial \bar{\pi}}{\partial x_i} + g\delta_{i3}\bar{T} + \nu\frac{\partial^2 \bar{u}_i}{\partial x_j \partial x_j} + \frac{\partial K_{SGS}\bar{S}_{ij}}{\partial x_j} \tag{12a}$$

$$\frac{\partial \bar{T}}{\partial t} = -\frac{\partial \bar{u}_j \bar{T}}{\partial x_j} - \bar{u}_3\frac{dT_s}{dx_3} + \kappa\frac{\partial^2 \bar{T}}{\partial x_j \partial x_j} + \frac{1}{Pr_t}\frac{\partial}{\partial x_j}\left(K_{SGS}\frac{\partial \bar{T}}{\partial x_j}\right) \tag{12b}$$

$$\frac{\partial \bar{u}_i}{\partial x_i} = 0, \tag{12c}$$

where $\bar{\pi}$ is the pressure head fluctuation, which includes the GS and SGS normal stresses, or

$$\bar{\pi} = \bar{p} + \frac{\tau_{kk}}{3} + \frac{\bar{u}_k\bar{u}_k}{2}; \tag{13}$$

$\bar{u}_k\bar{u}_k/2$ is the GS KE and $\tau_{kk}/3$ is the SGS KE.

Smagorinsky's (1963) eddy viscosity formulation is used with a modification that takes into account the buoyant production of SGS energy (e.g., Eidson 1985; Siegel 1988; Lilly 1989; Mason and Derbyshire 1990). The SGS eddy viscosity, K_{SGS}, is derived assuming that it depends only upon the smallest resolvable scale (Δ) and the rate at which KE is transferred from scales larger than Δ to those scales smaller than Δ. Within the inertial subrange of turbulence, spectral transfers of kinetic energy past any given scale are equal to the KE dissipation rate, ϵ. Applying only dimensional arguments, K_{SGS} is given by

$$K_{SGS} = (c_s\Delta)^{4/3}\epsilon^{1/3}, \tag{14}$$

where the constant of proportionality (c_s) is denoted as the Smagorinsky constant. To evaluate the value of K_{SGS} at any point in space, the energy transfer rate (ϵ) must be known. In general, ϵ depends on all scales of motion. However, the SGS parameterization must be determined by the resolved scales alone. For a steady, statistically homogeneous flow, the dissipation of KE is equal to its production by shear and buoyancy processes. In nondimensional form, this "production equals dissipation" budget may be expressed as

$$\epsilon = -\frac{1}{2}\bar{S}_{ij}\tau_{ij} + g\delta_{i3}\tau_{\theta i}. \tag{15}$$

Here the dissipation of KE is balanced by the turbulent production by the GS shear ($-\frac{1}{2}\tau_{ij}\bar{S}_{ij}$) and by the SGS buoyancy fluxes ($g\delta_{i3}\tau_{\theta i}$). Applying the flux gradient forms of the SGS stresses (11) results in

$$\epsilon = \frac{1}{2}K_{SGS}\bar{S}^2 - \frac{g}{Pr_t}K_{SGS}\frac{\partial \bar{T}}{\partial x_3}, \tag{16}$$

where $\bar{S}^2$ is the mean square rate of strain ($=\bar{S}_{ij}\bar{S}_{ij}$). The value of K_{SGS} is found by substituting the scaling relation (14) for ϵ in terms of K_{SGS} into the kinetic energy budget (16). Solving for K_{SGS}, one can derive

$$K_{SGS} = \frac{(c_s\Delta)^2}{\sqrt{2}}\left(\bar{S}^2 - \frac{2g}{Pr_t}\frac{\partial \bar{T}}{\partial x_3}\right)^{1/2}$$

$$\bar{S}^2 > \frac{2g}{Pr_t}\frac{\partial \bar{T}}{\partial x_3}, \tag{17}$$

where the SGS eddy viscosity is set to zero if $\bar{S}^2$ is less than $2g/Pr_t\partial\bar{T}/\partial x_3$. The ratio of these two quantities defines a GS Richardson number (Siegel 1991). It should be noted that the inclusion of buoyancy forces did not significantly affect values of the SGS eddy viscosity (Siegel 1988). Thus, the SGS eddy viscosity may be determined knowing values for c_s and Pr_t.

Values of c_s used in previous large-eddy simulations of homogeneous turbulence, channel flow, Rayleigh–Bénard convection, and planetary boundary-layer turbulence vary from 0.13 to 0.24 (e.g., Deardorff 1974; Eidson 1982, 1985; Siegel 1988; Piomelli et al. 1989; Schumann 1991). Values of Pr_t used in LES experiments vary from 0.4 to 0.5 (Grötzbach and Schumann 1979; Grötzbach 1980; Eidson 1982). For the present experiments, a value of 0.15 is used for the c_s and a value of 1.0 is used for Pr_t. The choices for c_s and Pr_t were made primarily by comparing simulated spectral energy distributions with theoretical Kolmogorov–Obukhov (5/3) spectra. A series of experiments was done to examine the degree of correspondence between the simulated and theoretical radial wavenumber spectra and its relationship with variations in the values of c_s and Pr_t (Siegel 1988). The final values of $c_s = 0.15$ and $Pr_t = 1.0$ matched the theoretical spectra fairly well (Siegel 1988, 1991).

Implicit in the separation of GS and SGS motions is the assumption that the GS motions contain the energy of the flow, while the parameterized SGS processes dissipate this energy. Thus, a comparison of the GS and SGS energies, fluxes, and dissipation rates enables the performance of the SGS parameterization to be evaluated. A derivation of the SGS energy, dissipation, and fluxes is given in appendix A, while the performance of the SGS parameterization is assessed in section 10a.

5. Specification of initial conditions

A modification of the Garrett–Munk (GM) internal wave spectrum is used to initiate the present LES experiments (see appendix B). Spectral energy distributions are chosen to be consistent with GM energy levels, while the phases of each velocity and perturbation temperature component are selected randomly and not using linear internal wave theory (see below). This results in a highly chaotic initial condition from which the energetic decay may be observed. The thought is that the resulting initial flow fields have reasonably "oceanographic" energy levels without biasing the characteristic types of motion that would occur if a specific phase relationship were assumed (cf. linear internal waves, vortical motions, etc.).

It must be stressed that we are not attempting to initialize the present experiments with a "true" GM internal wave spectrum. There are many reasons why a "true" GM internal wave spectrum is inappropriate for the present experiments. For instance, planetary vorticity is not considered presently. Hence, inertial wave motions, an important component of the oceanic internal wave field, are excluded. In addition, the "true" GM spectrum does not correctly predict oceanic variance levels for vertical scales less than 5 m (e.g., Munk 1981); however, there is no other obvious choice. For example, the application of a Kolmogorov $k^{-5/3}$ energy spectrum will overspecify energy levels for scales larger than $\sim$1 m. Several other oceanographic wavenumber spectra, such as presented by Gargett et al. (1981) and Kunze et al. (1990), are inappropriate as they describe energy distributions only in a single direction. The choice of the GM spectrum for the shape of the initial energy distribution was made because it is, presently, the only unified, 3D wavenumber spectrum available.

The phases of the Fourier coefficients for each velocity component, $\hat{\mathbf{u}}(\mathbf{k})$, and the perturbation temperature, $\hat{T}(\mathbf{k})$, are chosen randomly for each vector wavenumber, $\mathbf{k}$. This is done instead of following linear internal gravity wave theory because it is unlikely that linear phase relations will hold for scales less than 10 m (e.g., Holloway 1983; Müller et al. 1986; Shen and Holloway 1986). The only phase constraint imposed is that the initial velocity field must be divergence-free ($\mathbf{k} \cdot \hat{\mathbf{u}}(\mathbf{k}) = 0$; see appendix B). If one were to initialize the flow field following linear internal wave theory, two additional phase constraints are imposed. Specifically, the initialized vorticity vector must lie in the horizontal plane ($\mathbf{k} \times \hat{\mathbf{u}}(\mathbf{k}) \cdot \mathbf{g} = 0$, where $\mathbf{g}$ is the gravitational acceleration vector) and the phase of the temperature perturbation must be in quadrature with the vertical velocity component. This means that a single random deviate is required to initialize the four components following linear wave phase relations. Here, the phase of the Fourier coefficients for each $\hat{\mathbf{u}}(\mathbf{k})$ and $\hat{T}(\mathbf{k})$ are chosen at random after which continuity is imposed. This choice of initial phases will not presuppose a particular wave-vortical character for the initial flow field (see section 7e). The analysis of the present results should provide directions for future LES experimentation.

A derivation of the *random-GM* initial conditions is presented in appendix B. Briefly, the GM spectrum assumes that the flow is characterized by horizontal isotropy, separable wavenumber and frequency dependence, random phase relations between linear internal wave modes, and a linear internal gravity wave dispersion relation (Munk 1981). The random-GM initialization also assumes that the nonhydrostatic approximation applies and that the velocity and temperature perturbation component phases are selected randomly.

The structure and temporal evolution of horizontal kinetic energy (HKE), vertical kinetic energy (VKE), and potential energy (PE) spectra are discussed in more detail in section 9 and hence, are only briefly addressed here. The initial energy in HKE and PE is primarily contained in low horizontal wavenumbers, while the distributions of these energetic components are nearly uniform in the vertical direction (Fig. 9a). Thus, the initial HKE- and PE-containing structures will be elongated in the horizontal and compressed in the vertical. The spectral energy distribution for VKE is more isotropic; however, its magnitude is considerably less. After a very short period of time ($Nt < 0.25$), the highly anisotropic initial wavenumber spectrum evolves into a more isotropic form (Fig. 9b). This rapid evolution is caused by both the attenuation of high wavenumber energy by the SGS dissipation parameterization as well as spectral transfers by nonlinear interactions. As the initial phases are randomized, nonlinear transfer processes are not initially active. After a short period of time ($<0.1Nt$), the nonlinear transfer processes become significant as measured by the magnitude of the velocity derivative skewness (e.g., Orszag and Patterson 1972). As expected, initial Reynolds numbers, based on the Taylor microscale (Re_λ), are large (3000–11 600) similar to values inferred from oceanographic observations. These initial Re_λ values are considerably larger than those simulated by direct numerical simulation methods ($\mathrm{Re}_\lambda < 100$).

6. Numerical methods

The complete description of the numerical procedure may be found in Siegel (1988), the following is

a brief synopsis of the methodology. The nondimensional domain size is 2π on a side, and resulting grid scale, Δ, is equal to $2\pi/M$ where M is the numerical resolution ($M = 64$). A discrete representation of the spatial coordinates (x_i) and the integer wavenumbers ($\mathbf{k}$; k_i; k_1, k_2, k_3; k_x, k_y, k_z) may be represented as

$$x_i = \frac{2\pi i}{M}, \quad i = 1, M \tag{18a}$$

$$k_i = i, \quad i = -M/2, M/2 - 1. \tag{18b}$$

The periodic boundary conditions simplify the numerics enabling pseudospectral techniques, based upon Fourier series expansions, to be applied (Orszag 1971a). Pseudospectral techniques perform computations in either physical or spectral space depending on where a given term may be most efficiently evaluated. This allows a high degree of computational convenience while retaining the inherent accuracy of a spectral computation (Orszag 1971b). Functions may be written in physical ($f(x_i)$) or spectral ($\hat{f}(k_i)$) space using discrete Fourier transforms:

$$f(x_i) = \sum_{|k_j|<K} \hat{f}(k_j) \exp(ik_j x_i) \tag{19a}$$

$$\hat{f}(k_i) = \frac{1}{(2\pi)^3} \sum_{|x_j|<2\pi} f(x_j) \exp(-ik_i x_j), \tag{19b}$$

where K is the maximum allowable wavenumber ($K = M/2$).

The evaluation of the nonlinear terms in the equations of motion by the pseudospectral method causes the resulting convolution sums to be contaminated by aliasing errors (Orszag 1971a). These aliased terms occur primarily in the corners of the wave vector box and are eliminated by a spectral truncation on the resulting velocity and temperature fields (Orszag 1971b; Canuto et al. 1988).

Time integration is performed using a leapfrog time stepping where the second-order viscous and diffusive terms are solved implicitly. The convective terms in the temperature equation are split into two parts using continuity to cancel aliasing terms that may arise in the scalar fields (J. J. Riley 1987, personal communication). The pressure head (13) is calculated diagnostically by solving the Poisson equation that arises after taking the divergence of the momentum equations and constraining the divergence of the velocity field of the $n + 1$ time step to be zero. This procedure insures that the flow field remains divergence-free.

The numerical experiments were performed on the Cray-XMP/48 at the San Diego Supercomputer Center. Each numerical experiment required 6.8 hours of CPU time to simulate 10 buoyancy periods (Nt). Each time step required about 10.2 seconds of CPU time at full resolution (64^3), with nearly 70% of the CPU time spent performing the calculations required by the SGS flux parameterization.

7. Time evolution of the domain-averaged statistics

a. Total energy decay

The temporal decay of the domain-averaged total energy nondimensionalized by its initial value (TE_0) is shown in Fig. 1a versus linear Nt, in Fig. 1b versus $\log_{10}(Nt)$, and in Fig. 1c in log-transformed dimensional time (minutes) for the three different stratifications ($N = 1$, 3, and 10 cph). In general, the value of TE/TE_0 decreases monotonically in time and faster for the $N = 1$ cph case than the others when viewed as a function of buoyancy time (Nt). When the variations of TE/TE_0 are compared as a function of dimensional time (Fig. 1c), the TE/TE_0 for the highly stratified case ($N = 10$ cph) decreases most rapidly. Thus, normalized total energy decay rates do not scale well either in buoyancy (Nt) or in dimensional time.

The observation that $N = 10$ cph TE/TE_0 decays the fastest in dimensional time and the slowest in buoyancy time can be explained by making a simple scaling argument. The total energy in the GM spectrum scales as N, requiring the initial velocity fluctuations (u') to go as $N^{1/2}$ (Munk 1981). An eddy viscosity for the *entire* initial flow field, K_e, can be formulated using Prandtl's mixing length hypothesis as $u'l$, where l is a characteristic length scale (Tennekes and Lumley 1972). The present LES observations indicate that l is not a strong function of N (Fig. 6) suggesting that K_e scales as $N^{1/2}l$. Assuming that TE decreases in time by eddy viscous processes ($d\mathrm{TE}/dt = K_e\nabla^2\mathrm{TE}$), the time rate of change for TE will scale as $N^{3/2}l^{-1}$. Thus, the decay rate for the *normalized* TE scales as $N^{1/2}$ in dimensional time and as $N^{-1/2}$ in buoyancy time. Thus, the normalized total energy for the $N = 10$ cph case decreases the fastest when viewed in dimensional time (Fig. 1c) and the slowest in buoyancy time (Fig. 1b).

The TE decay rate is often discussed by evaluating the exponent (n in a power law decay relation,

$$\mathrm{TE} \propto (Nt)^{-n}. \tag{20}$$

Numerical experiments of isotropic, decaying turbulence give values of n varying from 1.0 to 1.5 where the exact value is highly dependent upon the low wavenumber structure of the initial energy spectrum (e.g., Schumann and Patterson 1978a; Domaradzki and Mellor 1984; Lesieur 1987). Here, the decay exponent, n, appears to increase smoothly as a function of time (Fig. 1b). Values of n increase to about 1.4 for all three runs. Similar temporal variations in energy decay rates have been observed in direct numerical simulations of anisotropic turbulence (Schumann and Patterson 1978a). In particular, sharp reductions in TE decay rates are not observed, in contrast to what has been reported for previous laboratory and direct numerical experiments of decaying stratified turbulence (e.g., Dickey and Mellor 1980; Stillinger et al. 1983; Métais and Herring 1989).

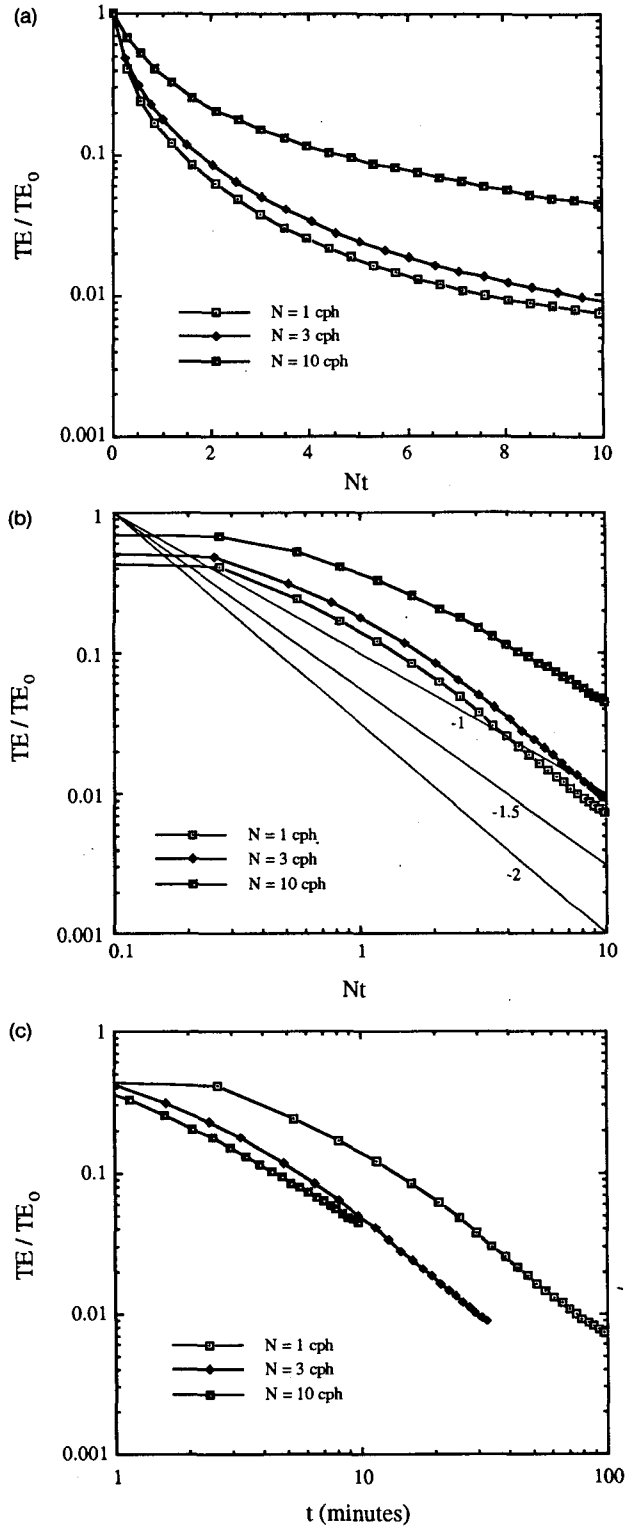

FIG. 1. Temporal variations of the nondimensionalized total energy (TE/TE$_0$): (a) TE/TE$_0$ vs Nt, (b) TE/TE$_0$ vs $\log_{10}Nt$, and (c) TE/TE$_0$ vs $\log_{10}t$ (dimensional time, minutes) are shown. Data for the three stratifications (N = 1, 3, and 10 cph) are shown. Note, the sloping thin lines in (b) represent decay exponents of 1.0, 1.25, and 1.5 in the power law relation for TE vs Nt (20).

b. Temporal evolution of flow energetics

For decaying, homogeneous, uniformly stratified turbulence, evolution expressions for the domain-averaged energy components (HKE, VKE, and PE) may be written symbolically as

$$\frac{d\text{HKE}}{dt} = \Phi_H - \epsilon_H, \quad \text{HKE} = \langle u^2 + v^2 \rangle/2 \tag{21a}$$

$$\frac{d\text{VKE}}{dt} = \Phi_V - \epsilon_V + \text{BF}, \quad \text{VKE} = \langle w^2 \rangle/2 \tag{21b}$$

$$\frac{d\text{PE}}{dt} = -\epsilon_P - \text{BF}, \quad \text{PE} = g^2\langle T^2 \rangle/2, \tag{21c}$$

where ϵ_H, ϵ_V, and ϵ_P are the respective energy dissipation rates, Φ_H and Φ_V are the pressure-strain correlation terms, and BF is the buoyancy flux ($\equiv g\langle wT \rangle$). The angle brackets are used to denote a domain average. Note that the triple product terms disappear when domain-averaged energy budgets are evaluated for a homogeneous flow (e.g., Tennekes and Lumley 1972). The pressure–strain correlation terms, Φ_H and Φ_V, are defined as

$$\Phi_H = \left\langle p\left(\frac{\partial u}{\partial x} + \frac{\partial v}{\partial y}\right)\right\rangle \tag{22a}$$

$$\Phi_V = \left\langle p\frac{\partial w}{\partial z}\right\rangle, \tag{22b}$$

where $\Phi_H + \Phi_V = 0$ as a result of continuity. A schematic diagram illustrating the interchanging of component energetics is shown in Fig. 2. The BF and the pressure–strain correlation terms (Φ_H and Φ_V) exchange energy among the three components (HKE, VKE, and PE). However, these terms play no role in the evolution of the total energy (TE) as

$$\frac{d\text{TE}}{dt} = -\epsilon_H - \epsilon_V - \epsilon_P = -\epsilon - \epsilon_P. \tag{23}$$

Thus, the TE of a decaying, stratified flow will monotonically decrease in time due to molecular dissipation processes (Fig. 1).

Temporal variations of domain-averaged HKE ($\langle \bar{u}^2 + \bar{v}^2 \rangle/2 + 2\text{KE}_{\text{sgs}}/3$), VKE ($\langle \bar{w}^2 \rangle/2 + \text{KE}_{\text{sgs}}/3$), and PE ($g^2\langle \bar{T}^2 \rangle/2 + \text{PE}_{\text{sgs}}$) are shown in the upper panel of Figure 3 for the three different mean stratifications. Derivation of the SGS energy levels (KE_{sgs} and PE_{sgs}) is given in appendix A. It should be noted that the SGS energy levels are always much less than the GS energetics (see section 10a). In general, HKE is greater than either PE or VKE and PE is greater than VKE with this difference increasing with increasing stratification. Note also that an equipartition does not exist between PE and the total amount of KE as would be expected for a superposition of linear internal gravity waves (e.g., Phillips 1980).

The time evolution of the three component energies display significant oscillations while decaying. In particular, VKE and PE exhibit strong oscillations, which are out-of-phase with each other. These oscillations start after an Nt of ~ 3 with a characteristic oscillation period of roughly 3 Nt, as expected for linear internal gravity waves. The VKE and PE oscillations are created by the temporal variations in the buoyancy flux, BF. Weak oscillations are also observed in the evolution of HKE, particularly for the higher stratification case (N = 10 cph; Fig. 3c), suggesting that the pressure strain correlation terms (which transfer energy between VKE to HKE; Fig. 2) are dynamically significant when the ambient stratification is intense.

c. *Internal waves, mixing, and the buoyancy flux*

Energy exchanges between VKE and PE are performed by the buoyancy flux, which when negative acts to convert VKE to PE. The temporal evolution of the domain-averaged BF ($g\langle \bar{w}\bar{T}\rangle + \mathrm{BF}_{\mathrm{sgs}}$, where $\mathrm{BF}_{\mathrm{sgs}}$ is the SGS BF) is shown in the second panel of Fig. 3. Large BF oscillations start after an Nt of about 2 and follow the variations in VKE and PE such that when BF is positive, decay rates for VKE decrease while those for PE increase. After an Nt of ~ 2, the BF exchanges PE and VKE in a nearly reversible, sinusoidal pattern with an oscillation period of roughly 3 Nt.

The evolution of BF is strongly modulated by VKE and PE levels as can be shown by examining a schematic BF budget

$$\frac{d\mathrm{BF}}{dt} = 2(\mathrm{PE} - \mathrm{VKE}) - g\left\langle T\frac{\partial p}{\partial z}\right\rangle + f(\nu, \kappa), \quad (24)$$

where $f(\nu, \kappa)$ represents various viscous and diffusive terms, which are not directly important for high Reynolds number turbulence. An excess of PE over VKE should cause an increase in BF, which in turn will act to reduce PE (21c). This coupling of PE and VKE via the BF gives rise to nearly reversible, wavelike oscillations in the domain-averaged energetics by driving internal gravity waves, especially after an Nt of ~ 2 (Fig. 3). However, these internal waves cannot be simply linear internal gravity waves (Stewart 1969), as a superposition of linear waves will produce a zero BF.

Evidence of an irreversible character for BF may also be observed. That is, when the irreversible portion of the buoyancy flux is negative, VKE is being permanently converted to PE, effectively raising the center of mass of the fluid while mixing temperature fluctuations down the mean temperature gradient. Irreversible aspects of the domain-averaged BF are best illustrated by examining the time-integrated buoyancy flux (IBF), or

$$\mathrm{IBF} = \int_0^{Nt} \mathrm{BF}(t')dt'. \quad (25)$$

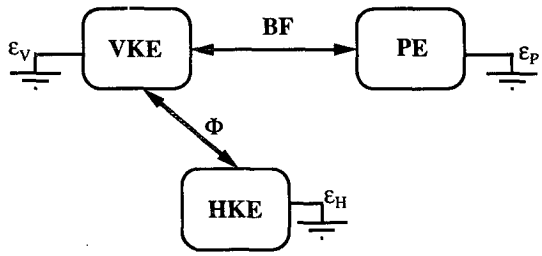

FIG. 2. Schematic diagram of the component energy exchanges in a statistically homogeneous, stably stratified fluid. Symbols are defined in the text.

Temporal variations of the temporally integrated buoyancy flux are shown in the bottom panel of Fig. 3. Early in the simulations ($Nt \leq 3$), the IBF rapidly accumulates negative values. After this initial period ($\sim 2Nt$), the rate at which IBF values decrease dramatically slows as it begins to oscillate. The transition between the strongly irreversible accumulation of PE and the reversible BF oscillations occurs suddenly and indicates that the initial turbulent flow evolves rapidly into a buoyancy-affected flow field dominated by internal wave motions. This transition is most striking for the lower N value experiments (N = 1 and 3 cph; Figs. 3a,b) than for the 10 cph case (Fig. 3c). However, for the high stratification experiment, the IBF is negative indicating that the BF is irreversible to some degree.

An irreversible character for BF can still be observed even after the BF transition for the Nt = 1 and 3 cph experiments. For these experiments, the IBF slowly decreases after an Nt of ~ 2, indicating the permanent accumulation of PE and down gradient mixing. The irreversible portion of BF ($\langle \mathrm{BF}\rangle_{\mathrm{I}}$) can be crudely estimated by determining the linear slope of the IBF versus Nt (after Nt = 2). The resulting regression slopes, $\langle \mathrm{BF}\rangle_{\mathrm{I}}$, may be expressed in terms of a vertical eddy diffusivity, K_ρ, by recognizing that K_ρ is defined as $-\langle \mathrm{BF}\rangle_{\mathrm{I}}/N^2$. The resulting values of K_ρ, in dimensional form, are 2.4×10^{-5} m^2 s^{-1} and 7.2×10^{-5} m^2 s^{-1} for the N = 1 and 3 cph experiments, respectively. These values are in the range expected for vertical mixing coefficients for the ocean thermocline ($10^{-6} \leq K_\rho \leq 10^{-4}$ m^2 s^{-1}; e.g., Munk 1966, 1981; Osborn and Cox 1972; Osborn 1980; Gregg 1989; Moum 1990).

Even though the present estimates of vertical eddy diffusivity produce realistic values, there are some caveats that must be addressed. For instance, as the flow decays, it is likely that the value $\langle \mathrm{BF}\rangle_{\mathrm{I}}$ should also decrease in time. Thus, the assumption that the value of $\langle \mathrm{BF}\rangle_{\mathrm{I}}$ is constant over the interval of Nt = 2 to 10 will be in error to some unknown degree. Also, the partitioning of the BF into reversible and irreversible components is purely heuristic based only upon our observations of the temporal evolution of IBF. Finally,

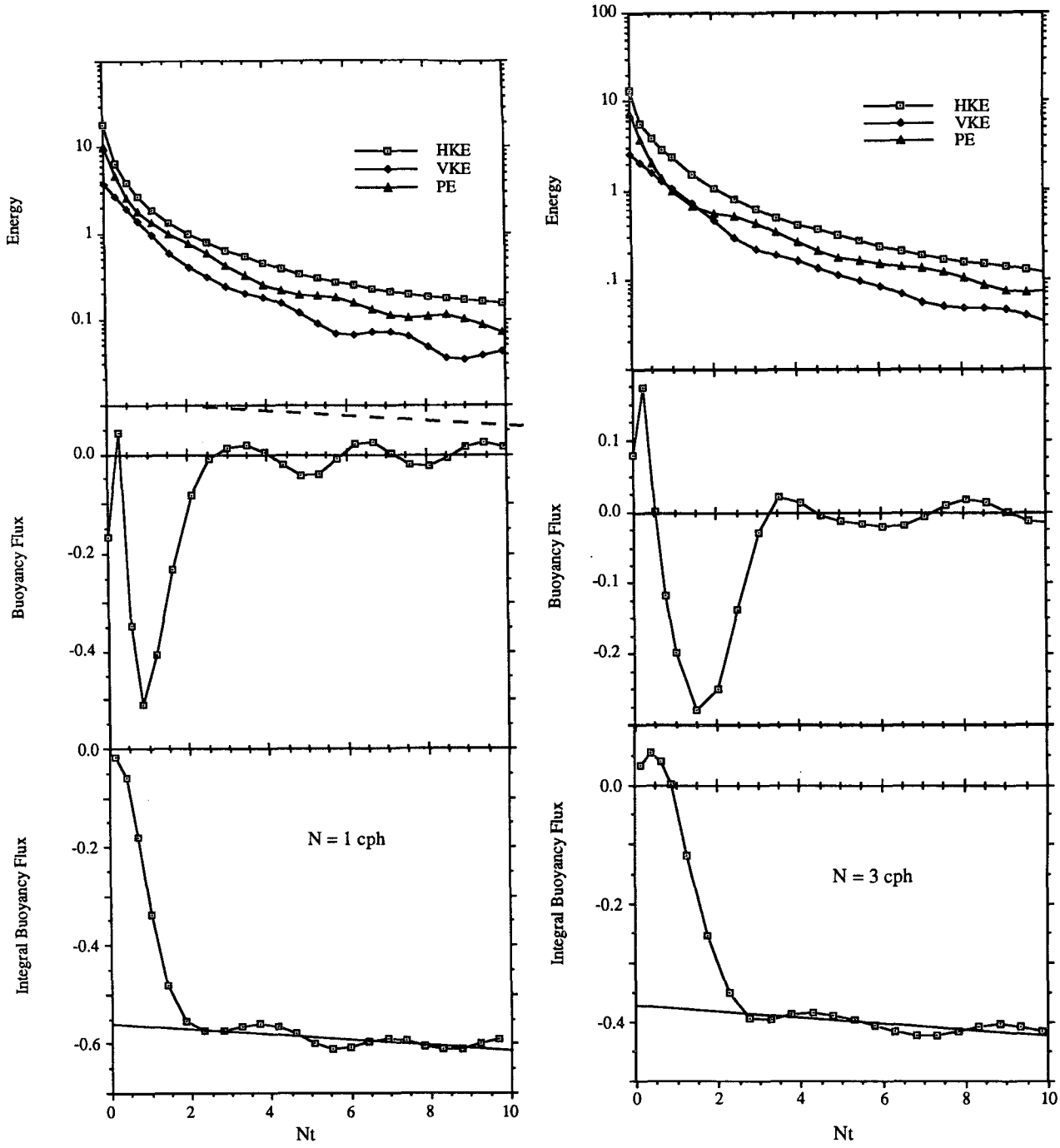

FIG. 3. Temporal variations of component energy levels (HKE, VKE, and PE), the buoyancy flux (BF), and the temporally integrated buoyancy flux (IBF) for mean stratifications of (a) $N = 1$ cph, (b) $N = 3$ cph, and (c) $N = 10$ cph. The straight lines through the IBF for the $N = 1$ and 3 cphs cases are least-squares fits of $\hat{\text{IBF}} = aNt + b$, where the constant a is interpreted as the irreversible component of the BF, $\langle \text{BF} \rangle_I$, for the flow after it is controlled by buoyancy processes. Insignificant correlations were found with the $N = 10$ cph case.

there remain questions in relating the simulated flow fields during their final period of decay to "true" ocean turbulence. However, the degree of correspondence of the K_ρ estimates with typical oceanographic values is encouraging.

d. Energy dissipation rates

Dissipation rates for KE and PE, ϵ and ϵ_P (defined in appendix A), decay monotonically in time and ϵ is always larger than ϵ_P (Fig. 4). Values of ϵ and ϵ_P de-

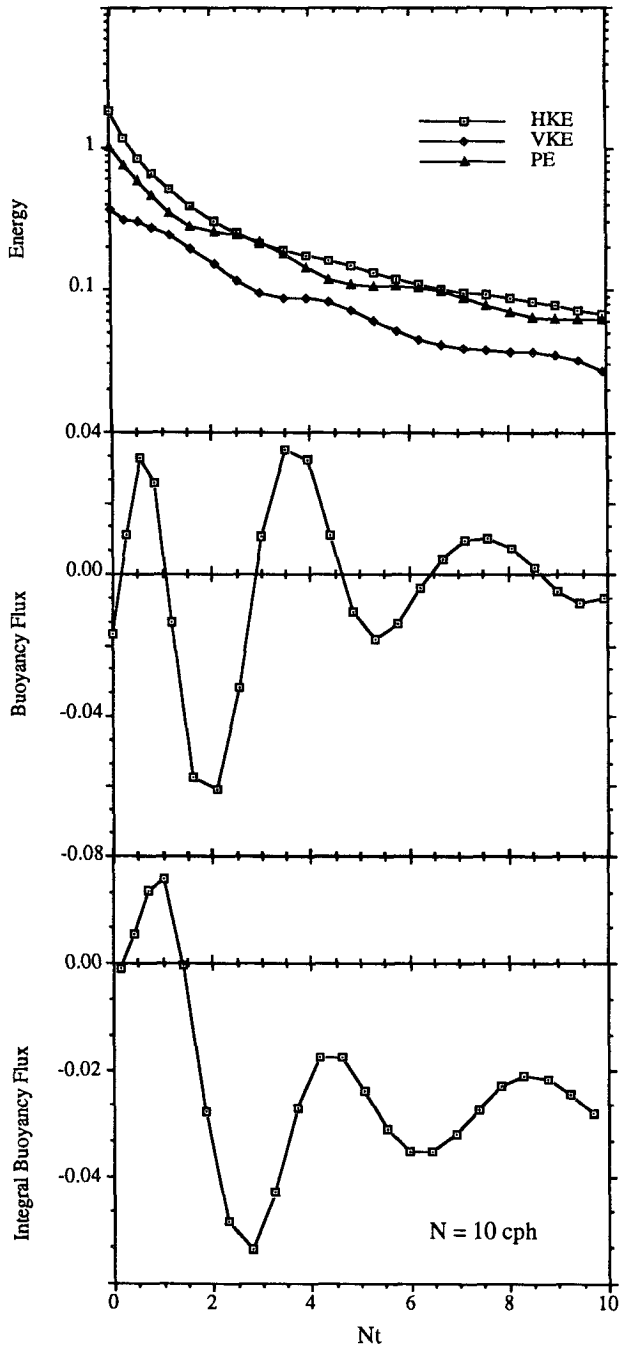

FIG. 3. (*Continued*)

crease about 2 to 4 orders of magnitude during the 10 Nt simulated, which is considerably more than the 1 to 2 orders of magnitude reduction in the component energy levels (Fig. 3). Weak temporal oscillations of ϵ and ϵ_P may be observed for the low stratification simulations (N = 1 and 3 cph), whereas insignificant oscillations in ϵ and ϵ_P are observed for the high stratification case (N = 10 cph). This indicates that internal wave processes are affecting primarily the larger, energy-containing scales of the flow as ϵ and ϵ_P emphasize the smaller scales of the simulated flow field (e.g., Tennekes and Lumley 1972; Lesieur 1987).

When normalized by νN^2, initial values of the nondimensionalized dissipation rate, $\epsilon/\nu N^2$, are large [$O(10^4)$], whereas values at Nt = 10 are typically much smaller (less than 100). Gargett et al. (1984) has suggested that $\epsilon/\nu N^2$ is a good indicator of the existence and extent of the turbulent inertial subrange. These relatively high values of $\epsilon/\nu N^2$ are consistent with the assumption that the GS cutoff is made within the inertial subrange of turbulence. The final values of $\epsilon/\nu N^2$ less than 100 are similar to observed values (e.g., Gregg 1989; Yamazaki 1990). The ratio of the PE and KE dissipation rates defines a mixing efficiency ($\eta = \epsilon_P/\epsilon$) for stratified turbulence (McEwan 1983). Values of η are between 0.20 and 0.25, roughly consistent with oceanic and laboratory observations (e.g., Oakey 1982; McEwan 1983).

e. Wave-vortex decomposition

The existence of a restoring buoyancy force acts to distinguish horizontal vortical motions from other motions. The wave–vortex (or Craya) decomposition is used to decompose the 3D velocity field into two scalar components. The distinction between these two scalar components as "wave" and "vortical" modes of motion is based upon kinematical considerations and is developed as follows (Fig. 5; Riley et al. 1981; Lilly 1983; Lesieur 1987; Müller 1988). In spectral space, each velocity vector, $\mathbf{u}(\mathbf{k})$, must lie in the plane perpendicular to its wave vector, $\mathbf{k}$, because of the continuity constraint ($\mathbf{k} \cdot \mathbf{u}(\mathbf{k}) = 0$). Thus, the velocity field may be completely described by two scalar fields. The wave-vortex decomposition is made by establishing one of the components as the projection of the velocity vector onto the horizontal plane (the vortical mode; u_v and v_v), while the residual is denoted as the wave component (u_w, v_w and w). An illustration of the relationships between a wavevector ($\mathbf{k}$), its velocity vector [$\mathbf{u}(\mathbf{k})$], and the results of the wave–vortex decomposition is shown in Fig. 5.

The interpretation of the wave-vortex decomposition is based upon several simple considerations. The vortex velocity vector (u_v, v_v, 0) is constrained to lie within a horizontal plane and thus cannot represent the vertical motions of an internal wave. The wave velocity vector (u_w, v_w, w) is not constrained to lie in any specific plane and hence, contains motions with components in all three directions. The vorticity vectors for the wave and vortex velocity components must be perpendicular to their respective velocity vectors and to the wavevector, $\mathbf{k}[\Omega(\mathbf{k}) = \mathbf{k} \times \mathbf{u}(\mathbf{k})]$. All of the vertical vorticity in the flow is contained in the vortex mode; however, the vortex component's vorticity is not purely vertical. The wave component vorticity is entirely in

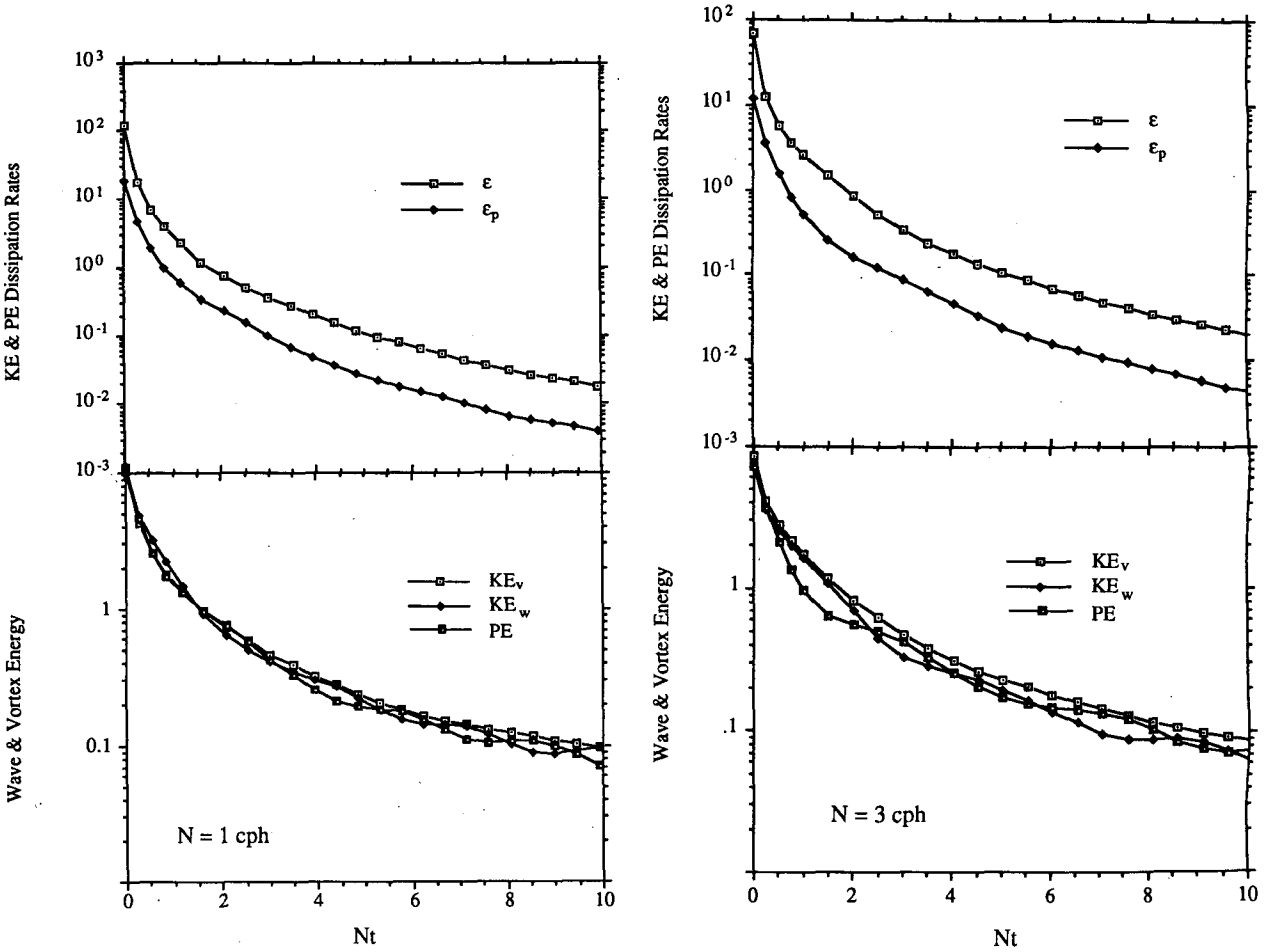

FIG. 4. Temporal variations of rates of KE and PE energy dissipation (ϵ and ϵ_P, respectively) are shown for mean stratifications of (a) N = 1 cph, (b) N = 3 cph, and (c) N = 10 cph. The evolution of the vortical kinetic energy (KE_v), wave kinetic energy (KE_w), and PE are shown in the lower panel of each plot.

the horizontal direction, similar to linear internal gravity waves. Thus, internal gravity waves will be represented by the wave component, whereas 2D vortices will contribute to the vortical mode.

It must be stressed that the wave–vortex decomposition is purely kinematical and does not imply a dynamical partition of the flow into waves and vortices. Obviously, this kinematical decomposition is, at best, only approximate; hence, its interpretation must be made cautiously. For example, a flow field with random phase relations between velocity components, such as fully developed turbulence, will have its kinetic energy equipartitioned between the wave and vortical forms. This will confound the interpretation of the wave-vortex decomposition in a flow field composed of vortices, internal waves, and 3D turbulence. However, for present purposes, the Craya decomposition provides a convenient, albeit approximate, means for evaluating the relative contributions of wave and vortex motions.

The temporal evolution of the vortical kinetic energy [$KE_v = (\langle \bar{u}_v^2 + \bar{v}_v^2 \rangle + KE_{sgs}/2)$], the wave kinetic energy [$KE_w = (\langle \bar{u}_w^2 + \bar{v}_w^2 + \bar{w}^2 \rangle + KE_{sgs}/2)$], and the potential energy (PE) is shown in the bottom panel of Fig. 4. In general, KE_v decreases monotonically with respect to time while KE_w and PE oscillate out-of-phase with each other. Temporal oscillations in the level of KE_v are not observed for any of the experiments supporting the ascription of the vortical component to 2D motions. The nearly identical energy levels and the tightly coupled evolution of KE_w and PE indicates that these two components are well equipartitioned in a global sense (i.e., averaged over all scales). This suggests that KE_w may be a good measure of the kinetic energy of the internal wave field. A similar equipartition has been observed in a direct numerical simulation (at low Re_λ) of stratified, decaying turbulence by Métais and Herring (1989). However, there is no sense of an equipartition between the vortical and wave kinetic energies (Fig. 4).

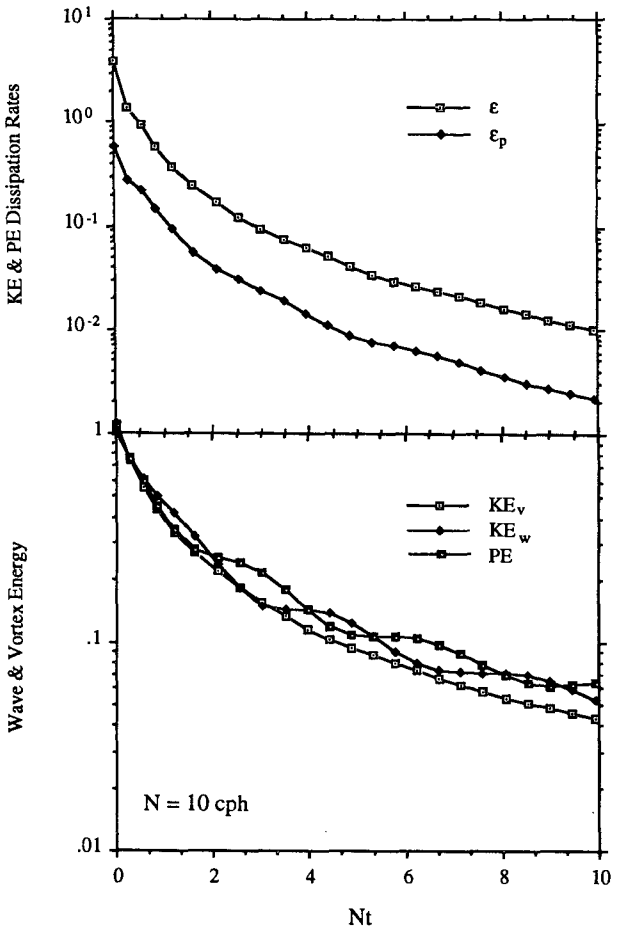

FIG. 4. (*Continued*)

f. Evolution of characteristic length scales

Length scales may be used to characterize the size of the energy-containing motions or the importance of particular processes in a turbulent flow (e.g., Tennekes and Lumley 1972). These scales may be defined using both dynamical and kinematical considerations. The derivation and interpretation of length scales for stably stratified flows has been made by many investigators in recent years (cf. Thorpe 1977; Gibson 1980, 1987; Dickey and Mellor 1980; Dillon 1982, 1984; Stillinger et al. 1983; Gargett et al. 1984; Itsweire et al. 1986; Crawford 1986; Gregg 1987; Métais and Herring 1989; Lienhard and Van Atta 1990; Yamazaki 1990; Barrett and Van Atta 1991). Here, many of these length scales are re-introduced so their notation and interpretation is clear.

Several length scales based upon dynamical considerations may be defined. For example, the Kolmogorov length scale (L_k) defines the scale at which molecular viscous and inertial forces are the same magnitude,

$$L_k = \left(\frac{\nu^3}{\epsilon}\right)^{1/4}. \tag{26a}$$

The direct effects of molecular viscosity are unimportant for present purposes as values of L_k are several orders of magnitude smaller than the GS cutoff (Δ; Siegel 1988). Another important dynamical length scale is the Ozmidov scale (L_0), which is defined using

$$L_0 = \left(\frac{\epsilon}{N^3}\right)^{1/2}. \tag{26b}$$

The Ozmidov scale represents the vertical length scale where the buoyancy forces affecting the evolution of vertical momentum are equal to the inertial (or nonlinear) terms. Vertical scales larger than L_0 will be affected by the ambient stable stratification, while those smaller will not. The wavelength scale (L_w) describes the vertical displacement of a fluid element that would occur if all of the VKE in the flow is transformed to PE. Here L_w is defined as

$$L_w = \frac{w'}{N} = \frac{(2\mathrm{VKE})^{1/2}}{N}, \tag{26c}$$

where w' is the root mean square of the vertical velocity.

Length scales based upon kinematical considerations may also be defined, such as the displacement scale (L_d), which quantifies the rms vertical displacement of a fluid parcel from its equilibrium position, or

$$L_d = \frac{\langle T^2 \rangle^{1/2}}{dT_s/dz}. \tag{26d}$$

Values of L_d have been used as an indicator of the largest turbulent scale assuming that the temperature fluctuations can be described using a geometric model of an overturning eddy (e.g., Stillinger et al. 1983; Gargett et al. 1984; Itsweire et al. 1986). However, internal wave processes also create vertical displacements of water parcels, particularly for the energy-containing

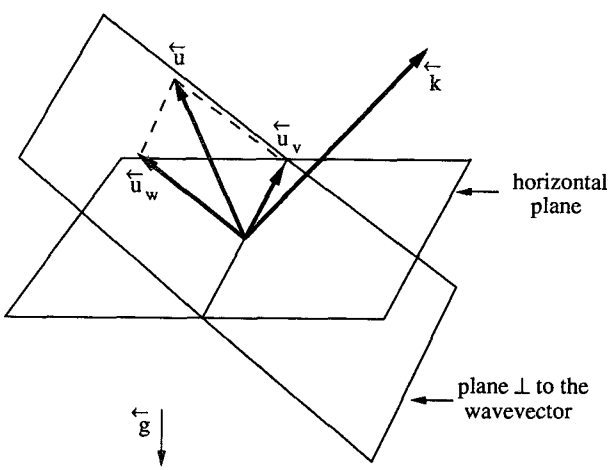

FIG. 5. Diagram in spectral space illustrating the wave-vortex decomposition of the velocity field into wave and vortical components (adapted from Müller 1984).

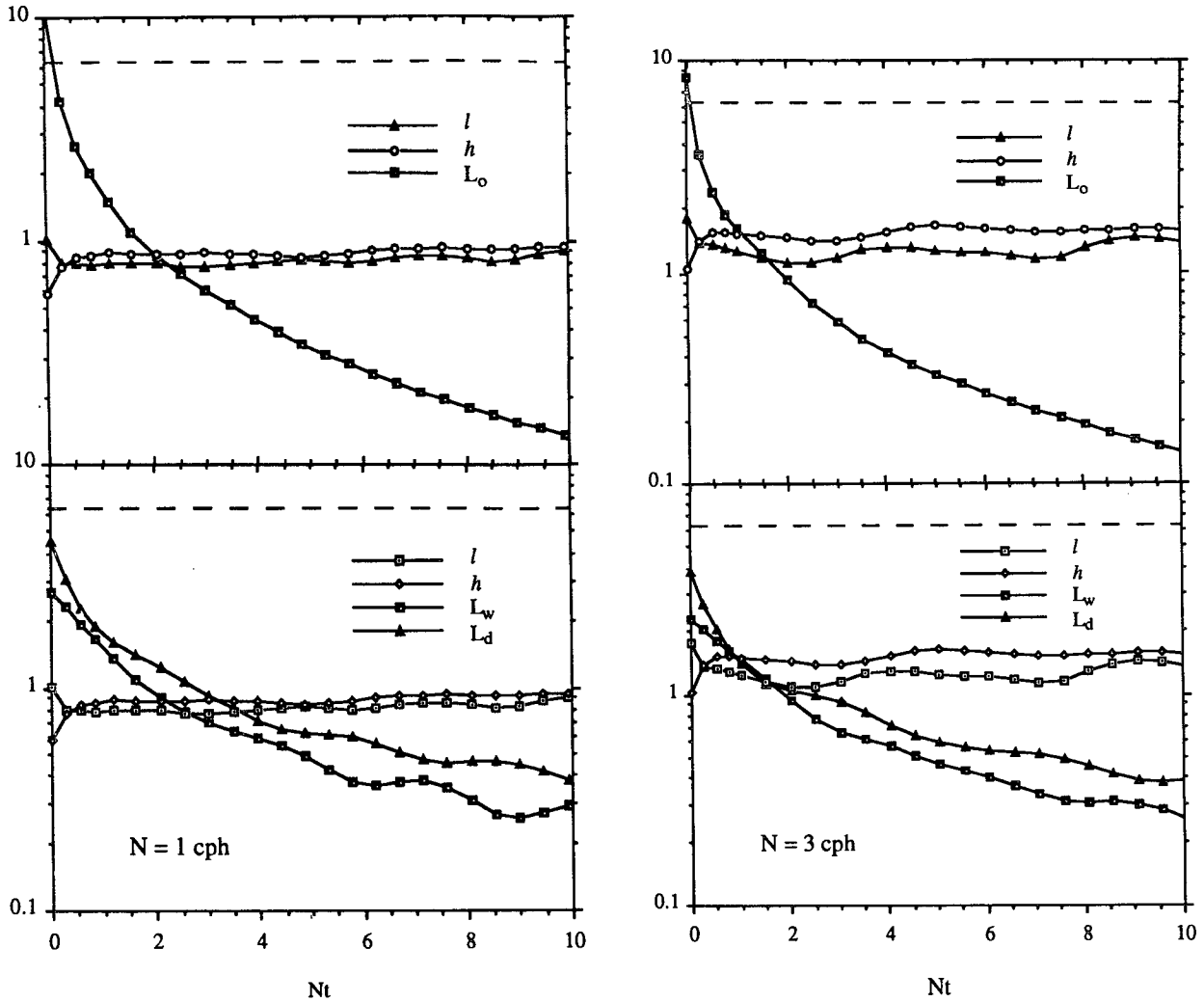

FIG. 6. The temporal evolution of vertical (h) and horizontal (l) energy-containing length scales and the Ozmidov scale (L_O) is shown in the upper panel for mean stratifications of (a) N = 1 cph, (b) N = 3 cph, and (c) N = 10 cph. The lower panel shows the evolution of the wave (L_w) and the displacement (L_d) scales, as well as the energy-containing scales (l and h). The horizontal dashed line in each panel represents the nondimensionalized size of the computational domain ($L = 2\pi$).

scales and variations in L_d should be interpreted with caution (e.g., Caldwell 1983; Yamazaki 1990).

Length scales characterizing the size of the energy-containing eddies (integral length scales) may be calculated directly using the 3D data. Integral length scales are calculated by evaluating the most probable length scale of the observed energy spectra (e.g., Monin and Yaglom 1981), or

$$L_{ij} = \frac{3\pi}{4}\left(\sum_{k_j=1}^{N/2} \hat{u}_i(k_j)\hat{u}_i(-k_j)/|k_j|\right) \times \left(\sum_{k_j=1}^{N/2} \hat{u}_i(k_j)\hat{u}_i(-k_j)\right)^{-1}, \quad (26e)$$

where $\hat{u}_i(k_j)$ here represents Fourier amplitudes of the ith component of the velocity field in the jth wavenumber direction. Of particular interest are the horizontal (l) and vertical (h) energy-containing scales, which are defined here using

$$l = (L_{11} + L_{21} + L_{31} + L_{12} + L_{22} + L_{32})/6 \quad (26f)$$

$$h = (L_{13} + L_{23} + L_{33})/3. \quad (26g)$$

The definitions of l and h are somewhat arbitrary as several other reasonable choices can be made (Métais and Herring 1989). The presently defined length scales relate to the horizontal and vertical extent of the KE-containing structures. It should be stressed that the definition of the integral scales (l and h) makes no distinction whether these structures are turbulent, internal wave, or vortical motions.

Comparisons among the various length scales are probably best made using a length scale evolution dia-

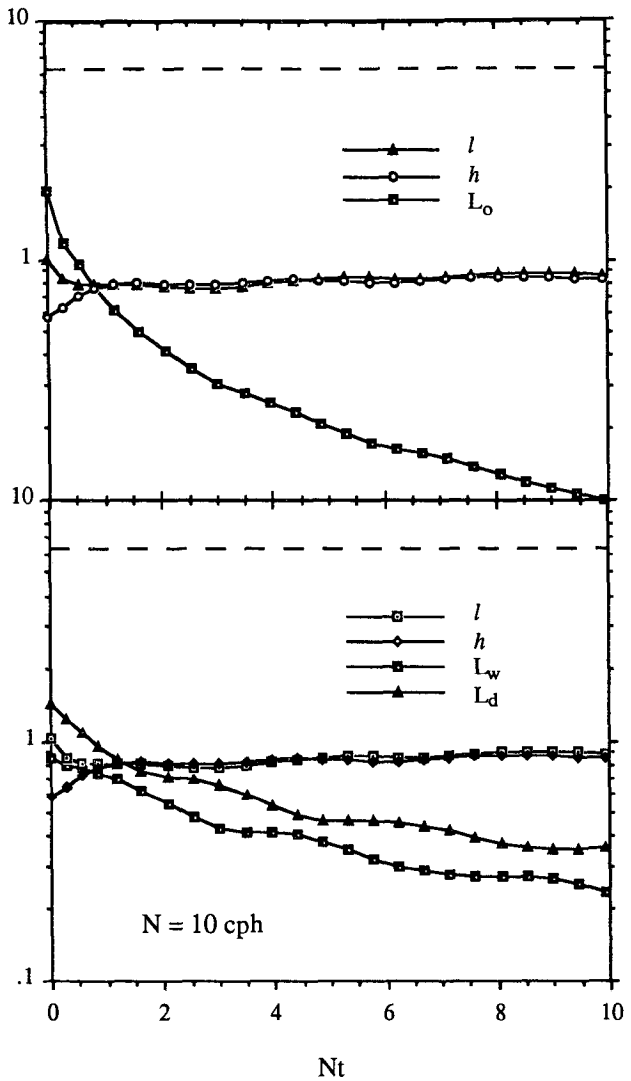

FIG. 6. (*Continued*)

gram (Stillinger et al. 1983). Examples of evolution diagrams for the Ozmidov and energy-containing scales (L_0, l, and h) are shown in the upper panel of Fig. 6 and for the wave, displacement, and energy-containing scales (L_w, L_d, l, and h) in the lower panel for the three different stratifications. The derived length scales may also be compared to the size of the computational domain ($L = 2\pi$; the dashed horizontal line) and the grid-scale cutoff ($\Delta = 2\pi/64 \approx 0.0982$; not shown).

In general, the horizontal and vertical energy-containing scales (l and h) remain uniform throughout the flow's evolution. Initially, l is larger than h as prescribed by the initial conditions. However, the integral scales quickly become roughly isotropic. There does not appear to be a significant trend in the size of either of the integral scales with stratification intensity. Nor does there appear to be a trend in the degree to which these scales are isotropically distributed.

The Ozmidov length scale (L_0) decreases rapidly with time (Fig. 6). Initially, L_0 is larger than either of the integral scales indicating that the vertical energy-containing scales are affected more by inertial forces than by buoyancy forces. Early in the flow's evolution, a transition occurs where the buoyancy forces begin to become important. This dynamical transition (when $h \sim L_0$) occurs at a buoyancy time (Nt) just less than one for the $N = 10$ cph case and at an Nt of 2 for the $N = 1$ cph case. This dynamical transition does not manifest itself in the evolution of integral scales, indicating that the size and vertical–horizontal structure of the kinetic energy-containing scales remain invariant through this transition. The timing of the length scale transition is similar to changes observed in the IBF evolution (Fig. 3). Further discussion of the consequences and role of this dynamic transition will be presented in section 10b.

The evolution of the vertical displacement scales, the wave scale (L_w) and the displacement scale (L_d), are compared to the magnitudes of the energy-containing scales (h and l) in the lower panels of Fig. 6. Values of L_d and L_w decrease in time while they oscillate similar to VKE and PE, as is expected (26c and d). Values of the ratio of L_d to L_w range from about 1.2 to 1.5 and increase in time. This indicates that the rms vertical displacement of isothermal surfaces is greater than could be produced by the instantaneous amount of VKE. Other energy sources besides VKE, such as HKE, must contribute energy to support the observed isotherm displacements where HKE is transferred to VKE via the pressure–strain correlation. This interaction of energy components is expected for internal gravity wave motions. In addition, the wave and displacement scales are both larger than the Ozmidov scale (L_0) for each experiment. This indicates that motions on these scales must have their vertical motions affected by buoyancy forces. Further, the evolution of L_w and L_d do not reflect the variations in h providing more evidence that these length scales are inappropriate for characterizing the size of the energetic structures in stably stratified turbulence.

8. Visualizations of the energetic structures

The visualization of the simulated three-dimensional velocity and temperature fields gives a visual depiction of the extent and orientation of the energetic structures. Vertical–horizontal cross sections of the horizontal kinetic energy [HKE(x, π, z)], the vertical kinetic energy [VKE(x, π, z)], the potential energy [PE(x, π, z)], and the absolute temperature profile [$\bar{T}(x, \pi, z) + T_s(z)$] for the $N = 1$ cph stratification experiment are shown in Fig. 7a at $Nt = 1$ and in Fig. 7b at $Nt = 5$. The $N = 1$ cph case is chosen as its BF evolution responds most acutely to the transition from an inertial to a buoyancy-dominated flow (Fig. 3a). Vertical–horizontal cross sections using data from the other

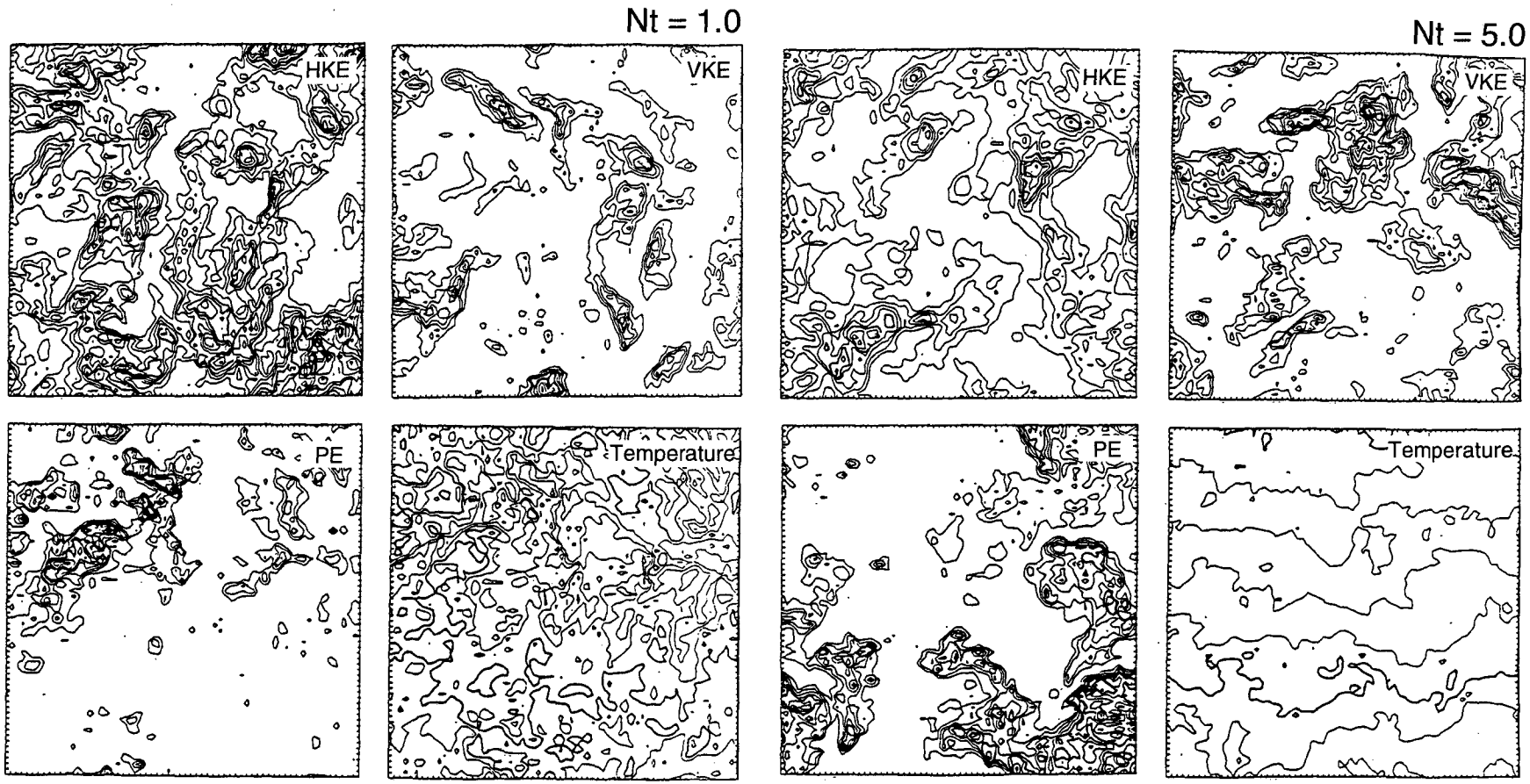

FIG. 7. Horizontal–vertical cross-sectional distributions of HKE(x, π, z), VKE(x, π, z), PE(x, π, z), and $\bar{T}(x, \pi, z) + T_s(z)$ for the $N = 1$ cph stratification at an Nt of 1 (a) and an Nt of 5 (b). Each tick mark on the axis corresponds to a computational grid point. The temperature contour interval is equivalent to 2 mK. Note, the contour level for HKE at $Nt = 5$ is one-half of the contour levels used for VKE and PE.

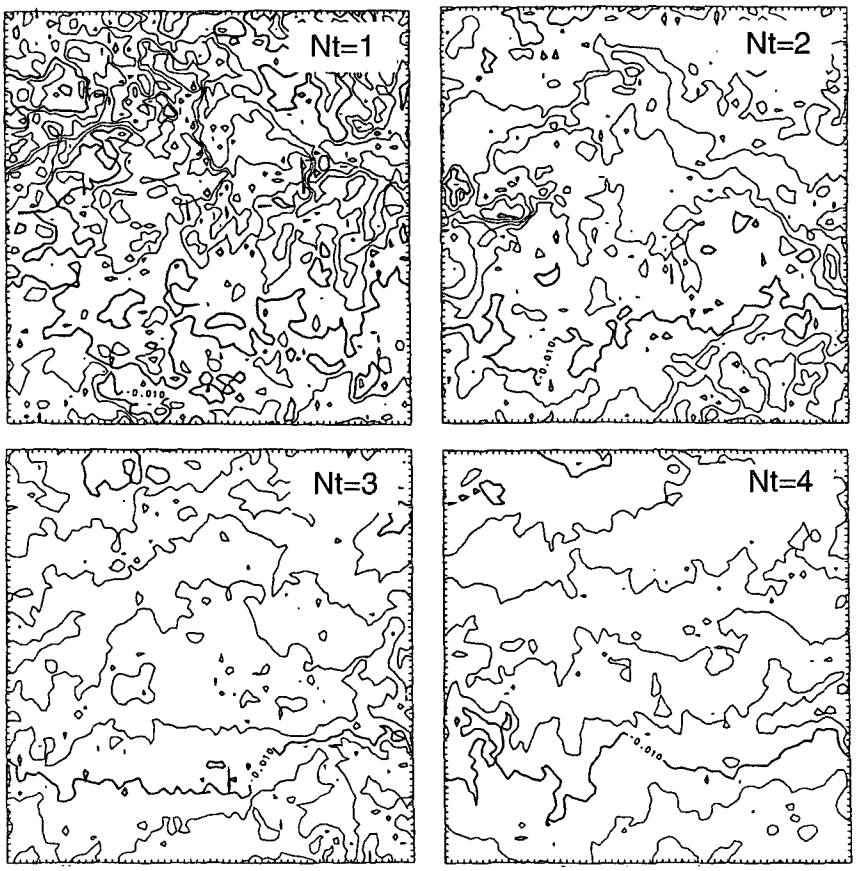

FIG. 8. Horizontal–vertical slices of $\tilde{T}(x, \pi, z) + T_s(z)$ for Nt = 1, 2, 3, and 4 for a mean stratification of N = 1 cph. The temperature contour interval is equal to 2 mK.

stratification cases are qualitatively similar (Siegel 1988).

In general, the HKE, VKE, and PE spatial structures are characterized by nearly equal vertical and horizontal dimensions. These structures are found intermittently in space, without any preferred orientation. There also appears to be little difference in the character of the HKE, VKE, and PE distributions between the two times, consistent with the evolution of the energy-containing length scales (h and l; Fig. 6a). This consistency in the energy containing structures is similar to the results of recent laboratory-based visualizations of active scalar distributions in decaying stratified turbulence (Barrett and Van Atta 1991). In particular, the KE or PE structures for the Nt = 5 maintain an aspect ratio of nearly one illustrating that there is little "pancaking" of the energetic structures after the vertical momentum balance becomes dominated by buoyancy processes.

In contrast to the energy distributions, vertical–horizontal cross sections of the absolute temperature profile show significant differences between Nt = 1 and Nt = 5 (Fig. 7). At Nt = 1, the temperature field is highly chaotic with many complicated, small-scale structures. However, at Nt = 5, the temperature structure shows considerably less variability and vertically coherent wavelike features are observed. Thus, a transition has occurred in the character of the vertical temperature profile. In addition, several temperature inversions are observed in the Nt = 5 temperature distribution with structures that are reminiscent of overturning Kelvin–Helmholtz instabilities. However, there appears to be little correspondence between these overturning structures and intense patches of VKE or HKE (Fig. 7b).

The transition between a fully turbulent flow and one dominated by buoyancy forces may be better visualized by examining the temporal evolution of vertical slices of the absolute temperature. An example of this temporal evolution is given for the N = 1 cph case for buoyancy times (Nt) of 1, 2, 3, and 4 in Fig. 8. These temperature distributions illustrate a highly turbulent flow gradually evolving into an internal wave–dominated flow, with the general features described above. This transition does not appear to occur at a specific time, unlike the evolution of the integrated buoyancy flux (Fig. 3a).

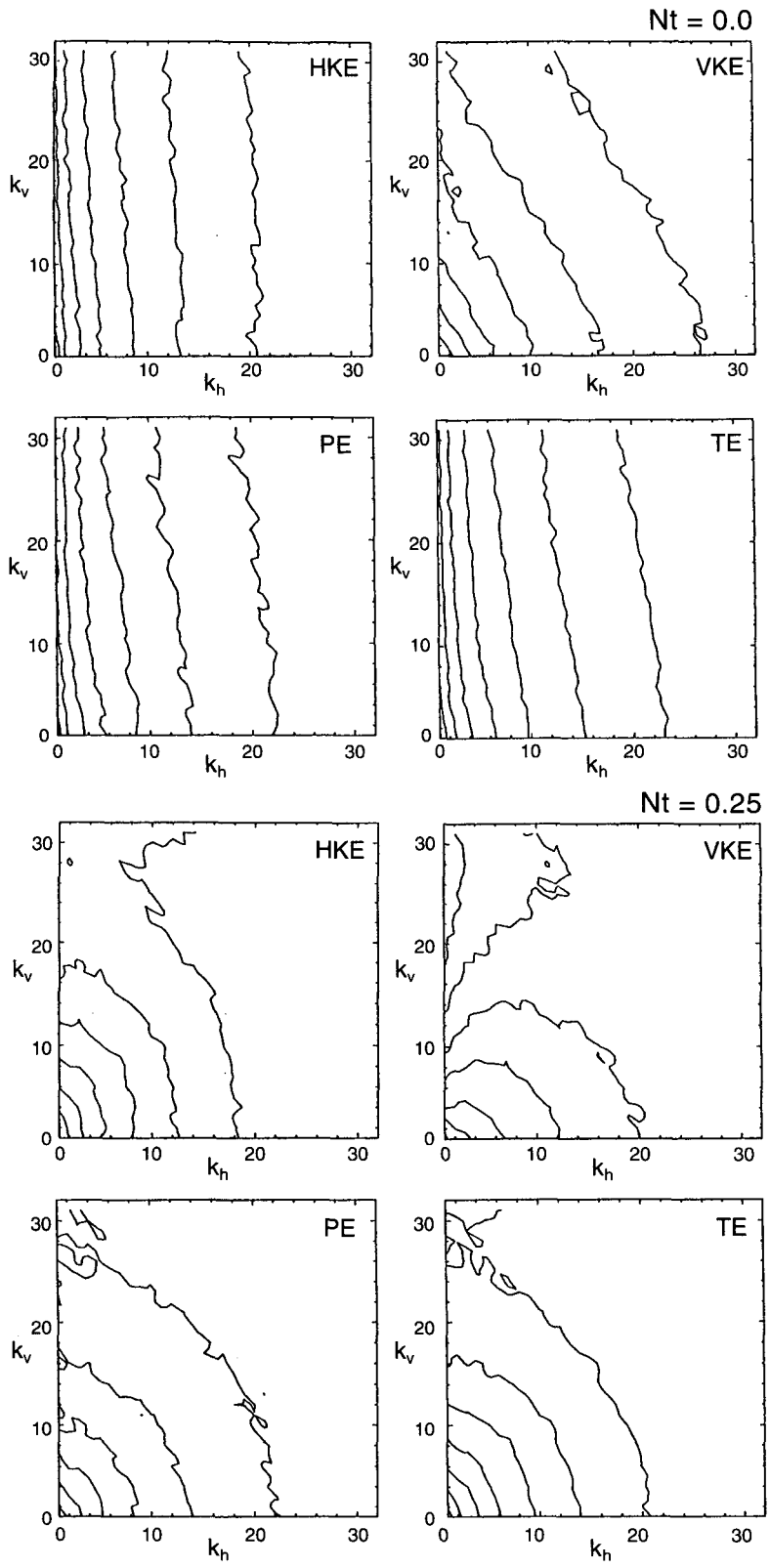

FIG. 9. Horizontal–vertical wavenumber distributions of horizontal kinetic energy [HKE(k_h, k_v)], vertical kinetic energy [VKE(k_h, k_v)], potential energy [PE(k_h, k_v)], and the total energy [TE(k_h, k_v)] for the N = 1 cph experiment. Buoyancy time (Nt) of (a) 0, (b) 0.25, (c) 1,

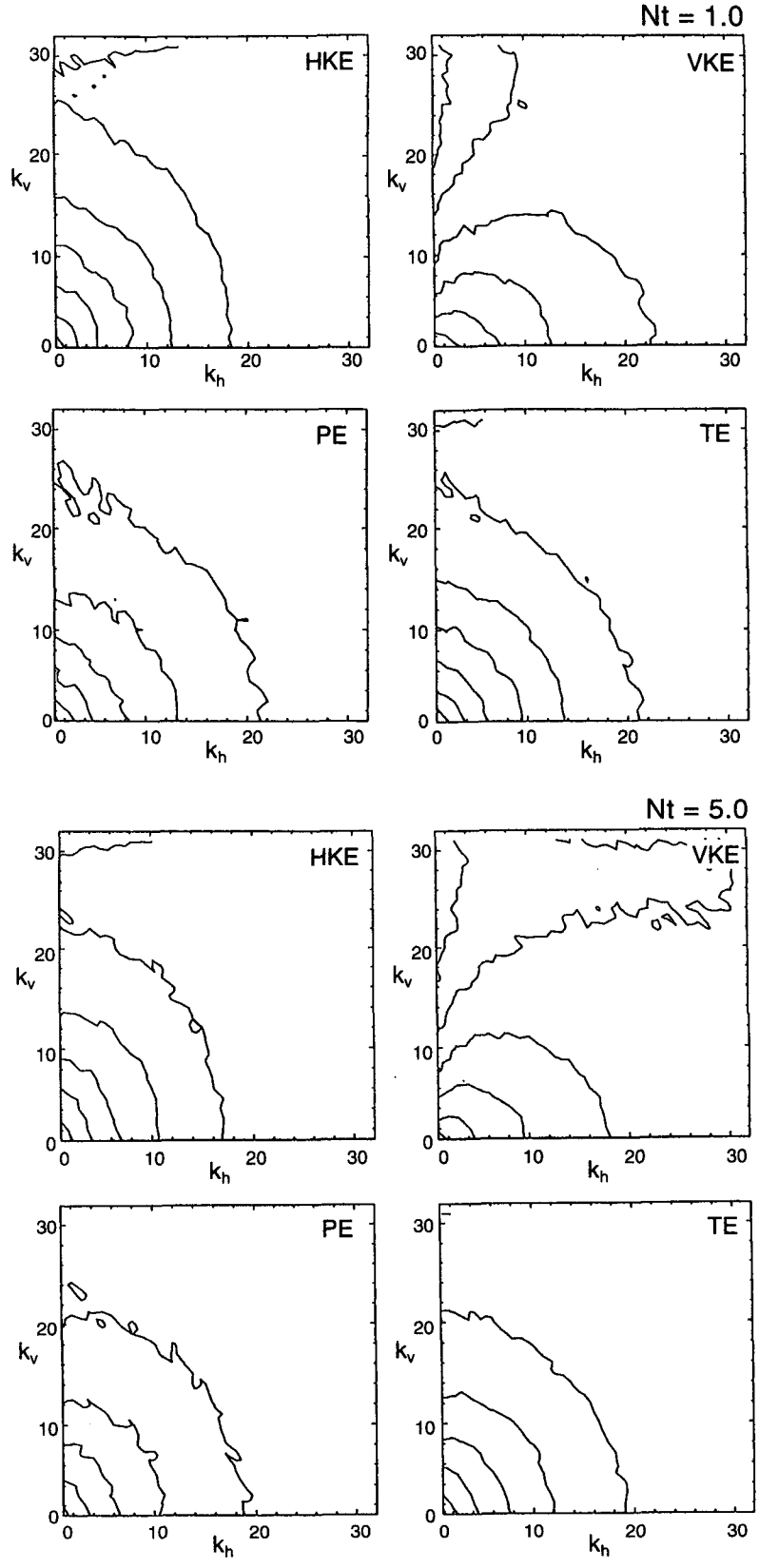

FIG. 9. (*Continued*) and (d) 5 are shown. Here, the distribution of the energy per mode (for each individual wavevector) is shown where the lines correspond to constant energy levels evenly spaced in units of $\log_{10}$(energy) and are scaled separately for each of the spectral distributions.

9. Spectral energy evolution

The development of anisotropy in the flow may be better examined using horizontal–vertical wavenumber distributions of spectral energy levels. Definitions and procedures used in making the spectral energy calculations are presented in appendix C. The two-dimensional representations for the horizontal kinetic energy [HKE(k_h, k_v)], vertical kinetic energy [VKE(k_h, k_v)], potential energy [PE(k_h, k_v)], and total energy [TE(k_h, k_v)] distributions are shown in Fig. 9 for Nt = 0, 0.25, 1, and 5. Again, only the N = 1 cph experiment is shown in an effort to assess the influence of the inertial-buoyancy transition on spectral energy distributions and transfer rates. Here, spectral distributions of energy per individual wave mode are shown where the isolines correspond to constant energy density and are scaled separately for each component (see appendix C). Using this representation, an isotropic energy distribution will have isolines of constant density at a fixed radial distance from the spectral origin.

Obviously, the initial spectra are highly anisotropic (Fig. 9a). Generally, HKE and PE are contained primarily in low horizontal wavenumbers, while energy is almost uniformly distributed over the vertical wavenumbers. Thus, the energy contained in the initial HKE and PE spectra have relatively large horizontal and small vertical scales. This characteristic was observed in the initial values of the energy-containing length scales (h and l; Fig. 6). As time proceeds, the spectral energy distributions evolve toward isotropic energy distributions. This redistribution occurs rapidly during the first 0.25 Nt (Fig. 9b), but some subsequent temporal evolution in the horizontal–vertical wavenumber distributions may still be observed (Figs. 9c and 9d). This evolution toward isotropy is particularly evident for the total energy distribution, which appears nearly isotropic by an Nt of 5. However, the component spectral energy distributions [cf. HKE(k_h, k_v) and VKE(k_h, k_v)] are not isotropically distributed. This result was also observed for the other two stratifications investigated (N = 3 and 10 cph).

The results of the wave–vortex decomposition may be evaluated spectrally in order to assess the global equipartition between the wave kinetic and potential energies (Fig. 4a) as well as investigating the scale dependency of "waves" and "vortices" from the Craya decomposition. Examples of KE_v, KE_w, and PE spectra for the vertical (k_v) and the horizontal (k_h) wavenumber shells (for N = 1 cph, Nt = 0, 1 and 5) are shown in Fig. 10. Initially, the KE_v and KE_w spectra are roughly the same as the total amount of kinetic energy is equipartitioned between these two forms. Spectral slopes are steeper in the horizontal direction ($\sim k^{-2}$) than in the vertical direction ($\sim k^{-1}$). After the initial reorganization (Nt = 1), the spectral slopes for both directions become more steep (just less than k^{-2}) where the slope of the PE spectra is less than the spectral slopes for either of the kinetic energy spectra. Generally, the energy spectra exhibit $k^{-5/3}$ regions in at least part of their resolved wavenumber ranges, although of course, the existence of a $k^{-5/3}$ is not necessarily indicative of the existence of an inertial subrange of turbulence (e.g., Lesieur 1987; Kerr 1990). Subsequent spectral energy evolution (Nt = 5) is much less than the initial reorganization (Fig. 10). Interestingly, a spectral equipartition between KE_w and PE does not appear to hold, although one is observed in the evolution of the domain-averaged KE_w and PE values (Fig. 4a). In some sense, a better equipartition is found between the KE_v and KE_w spectral distributions as expected for a purely random velocity field.

The relative contributions that vortical motions make to total energy (TE) spectrum may be evaluated by examining the spectral ratios of $3KE_v(k_v)$ to $TE(k_v)$ and $3KE_v(k_h)$ to $TE(k_h)$. These ratios will be equal to one if the flow is fully equipartitioned among the three components [i.e., $PE(k_v) \approx KE_w(k_v) \approx KE_v(k_v)$]. Therefore, this provides a reasonable method for assessing the relative contributions of vortical motions to the total energy spectrum. If the ratio of $3KE_v(\mathbf{k})$ to $TE(\mathbf{k})$ is greater than one, the total energy is composed of relatively more vortical energy than a fully equipartitioned field. Whereas, if the ratio of $3KE_v(\mathbf{k})$ to $TE(\mathbf{k})$ is less than one, there should be more wave energy [$PE(\mathbf{k}) + KE_w(\mathbf{k})$]. This simple interpretation is confounded by the coexistence of random 3D turbulent motions, as a random velocity field will be equipartitioned with equal vortical and wave kinetic energies. Thus, the presence of 3D turbulence will act to reduce spectral ratios of $3KE_v(\mathbf{k})$ to $TE(\mathbf{k})$.

Examples of these vortical-to-total energy ratios are shown in Fig. 11 for Nt = 1, 5, and 10 for the N = 1 cph experiment. Initially (Nt = 0), the ratios are spectrally uniform with values of about 1 (not shown). As time proceeds (cf. Nt = 1), values of this ratio reach about 1.1 for the wavenumbers ranging from 2 to 8 indicating relatively large contributions by vortical structures to the total energy of the flow for the larger scales simulated (Fig. 11). However, for the small simulated scales ($k > 7$), the ratios decrease to $\sim$0.7 indicating a dominance of internal wave and/or quasi-random, 3D turbulent motions. At Nt = 5, the difference in these ratios between these two spectral regions becomes significantly greater. Near the end of the simulation (Nt = 10), vortical energy structures contribute substantially to vertical and horizontal wavenumbers less than about 4, while the higher wavenumber region ($k > 7$) is deficient in vortical energy. In addition, the spectral extent over which vortical motions dominate the flow energetics decreases with increasing time indicating that vortical energy is being concentrated at larger scales as time proceeds (Fig. 10). This is particularly apparent in the horizontal direction. This concentration of vortical energy at larger spatial scales is reminiscent of

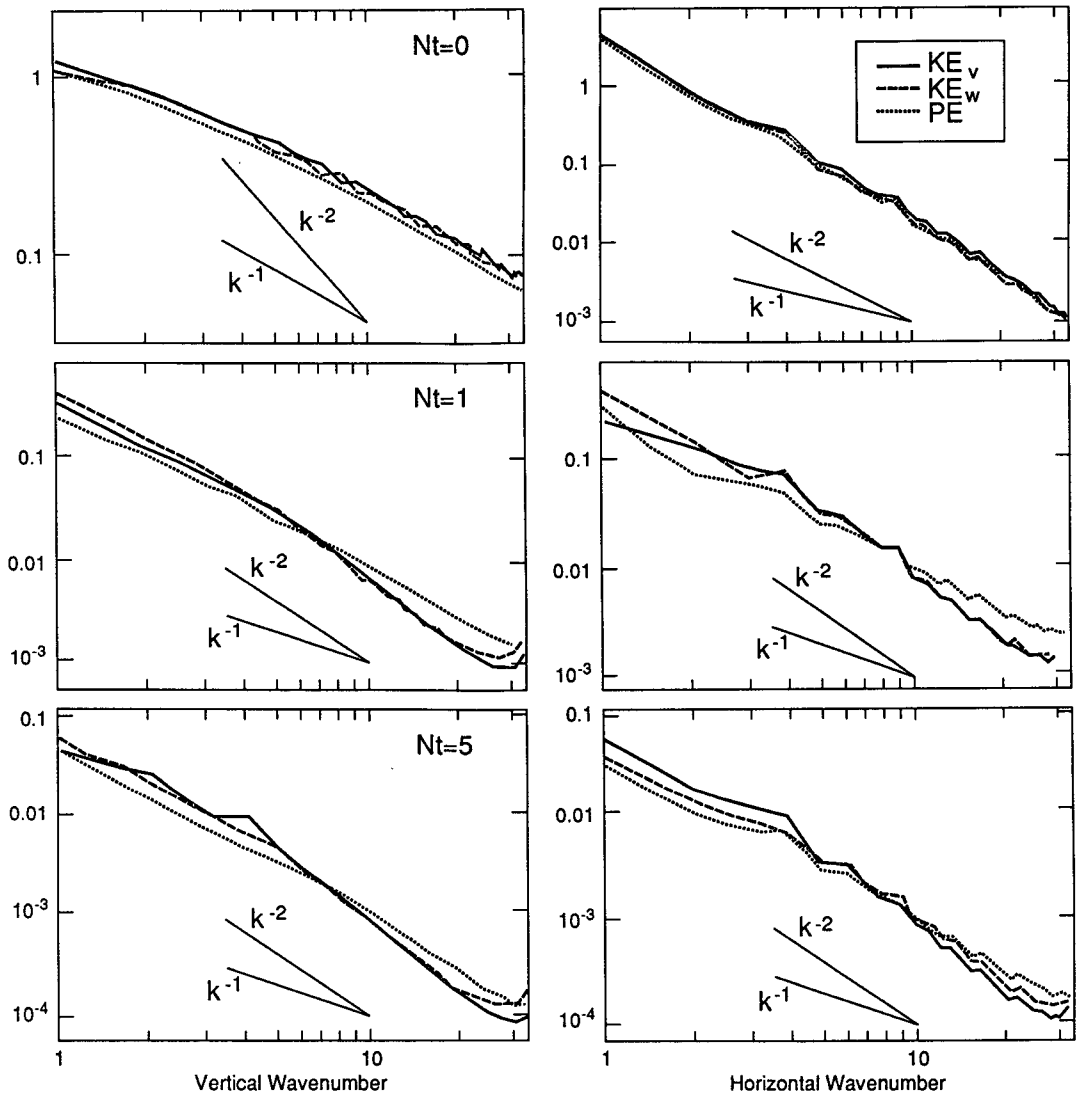

FIG. 10. Vertical (k_v; left side) and horizontal (k_h; right side) wavenumber spectra of vertical kinetic energy (KE_v; solid), wave kinetic energy (KE_w; dashed), and potential energy (PE; dotted) for $N = 1$ cph. Buoyancy times (Nt) of 0, 1, and 5 are shown. The lines in each panel represent k^{-2} (upper), k^{-1} (lower) spectral slopes.

the results of numerical simulations of decaying 2D turbulence where coherent vortices become larger and more isolated in time (e.g., Herring et al. 1974; Herring and McWilliams 1985). However, this is obviously not the case as the vortical modes addressed here are not true 2D vortices.

Details of the dynamic nature of the simulated motions and their temporal variations can be made by examining the spectral rates of nonlinear energy transfer. Rates of spectral horizontal kinetic energy transfer due to the nonlinear GS ($\hat{\Gamma}_{gs}(k_h)$) and the parameterized SGS processes ($\hat{\epsilon}_{sgs}(k_h)$) are shown in Fig. 12 evaluated in the horizontal wavenumber direction. Again, only data from the $N = 1$ cph experiment are shown. Derivation of rates of spectral energy transfer are presented in appendix D. Spectral energy transfer rates are nearly identical in the vertical direction (Siegel 1988).

In general, the GS nonlinear transfer terms, $\hat{\Gamma}_{gs}(k_h)$, remove energy from the lowest wavenumbers (generally less than 5) and add energy to higher wavenumbers (Fig. 12). These terms transfer energy spectrally from large to small scales as part of the turbulent cascade as energy must be conserved by nonlinear interaction processes. That is, the net effect of $\hat{\Gamma}_{gs}(k_h)$ when integrated over all scales of motion is identically zero (e.g., Lesieur 1987). In addition, there is no evidence of any back transfers of reverse energy cascades in $\hat{\Gamma}_{gs}(\mathbf{k})$, which are indicative of the enstrophy cascade in 2D turbulence. The SGS processes, $\hat{\epsilon}_{sgs}(k_h)$, act as

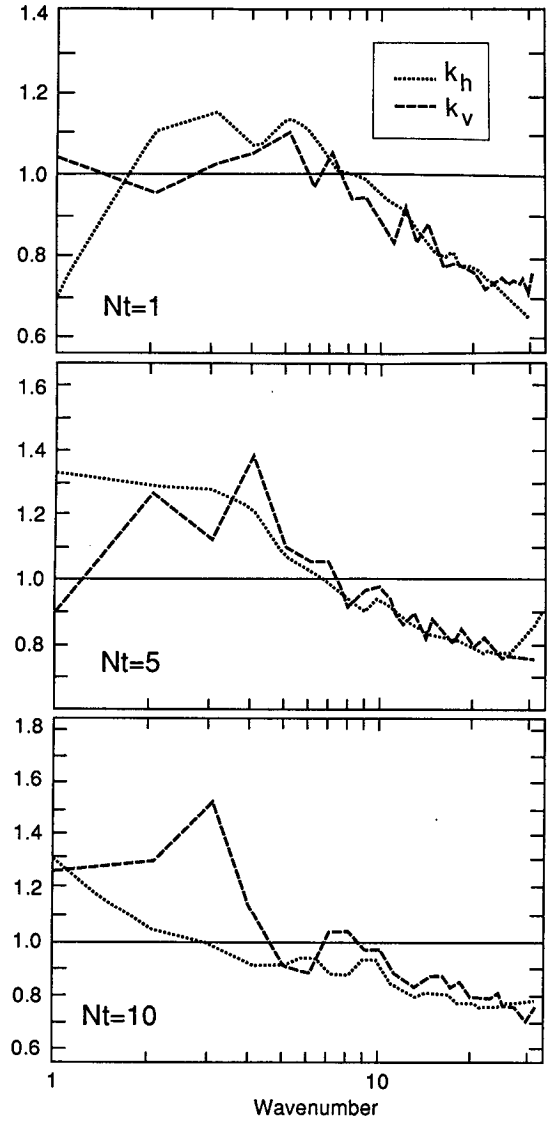

FIG. 11. Vertical (k_v; dashed) and horizontal (k_h; dotted) wavenumber spectra of the ratio of $3KE_v$ to TE for Nt = 1, 5, and 10 for the N = 1 cph experiment. Values greater than one indicate relatively more vortical than wave energy compared with a complete equipartition of energy among KE_w, KE_v, and PE (see the text).

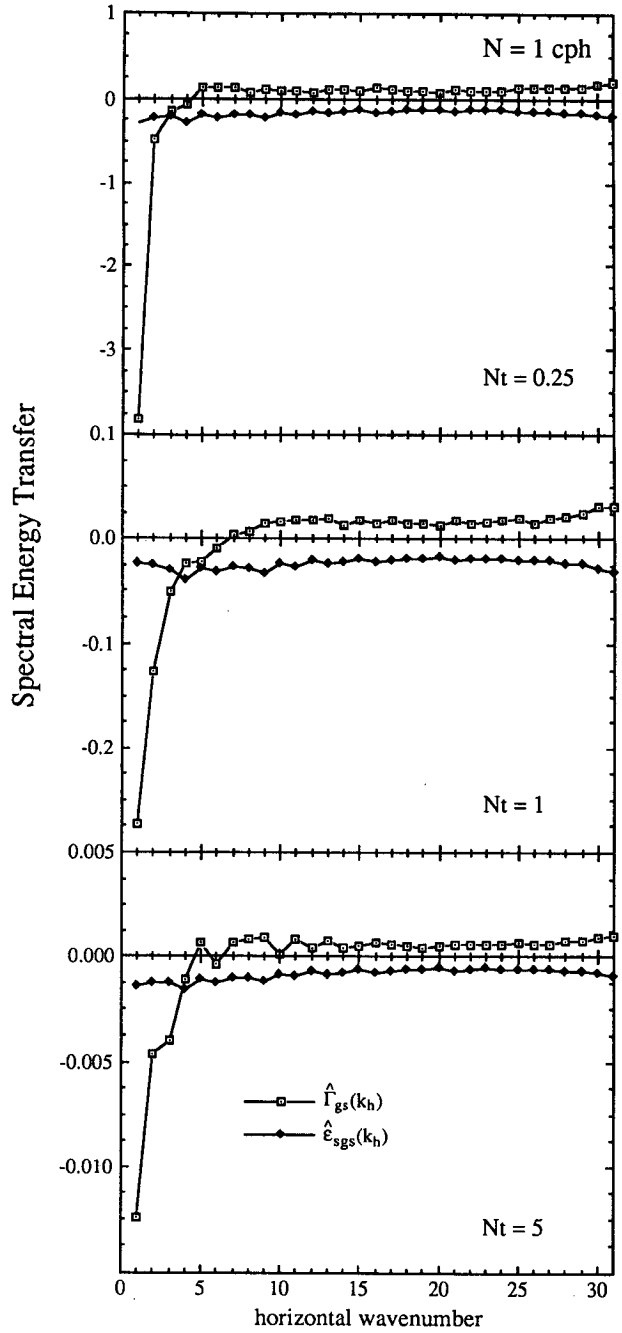

FIG. 12. Spectral energy transfer of HKE by nonlinear interactions [$\hat{\Gamma}_{gs}(k_h)$] and by parameterized SGS processes [$\hat{\epsilon}_{sgs}(k_h)$] for the N = 1 cph experiment. Procedures for calculating energy transfer spectra are given in appendix D. Buoyancy times (Nt) of 0.25, 1, and 5 Nt are shown. Spectra are shown only for the horizontal direction (k_h) although variations in the vertical wavenumber (k_v) direction are similar (Siegel 1988).

a spectrally uniform drain of energy (Fig. 12). Variations of $\hat{\Gamma}_{gs}(\mathbf{k})$ and $\hat{\epsilon}_{sgs}(\mathbf{k})$ in the vertical direction and for other energy components (VKE and PE) are similar (Siegel 1988).

For the smaller simulated spatial scales ($k > 10$), there exists a balance between the GS transfer and SGS drain terms (Fig. 12). For these scales, kinetic energy is transferred to small scales by resolved scale nonlinear interactions and this transferred energy in turn is then removed by the parameterized SGS processes. This coupled GS transfer–SGS dissipation process can be addressed conceptually in terms of the energy transfer processes for an inertial subrange. Within the inertial subrange, energy is transferred spectrally at a constant rate only by nonlinear interactions. Here, the parameterized SGS terms model the inertial cascade by re-

moving the amount of small-scale energy, which has been transferred to it by the GS nonlinear processes. If all of the scales of motion were resolved, these nonlinear cascades of energy would, of course, continue to molecular scales where viscous and diffusive processes would dissipate this energy. In effect, the SGS parameterization models the nonlinear cascading processes of the inertial subrange by removing the energy that GS processes have fed into it, modeling the expected nonlinear energy transfers of an inertial cascade.

10. Discussion

a. *Performance of the Smagorinsky SGS parameterization*

The evaluation of the performance of the SGS parameterization method is important for several reasons. First, verifying that the SGS parameterization has achieved its intended goal of modeling the effects of the unresolved motions will give greater confidence in the realism of the resolved scale flow fields. Second, improvements to the SGS model, both in modeling accuracy and in computational efficiency, may be found. These appraisals may be made in a number of different ways.

One such appraisal is testing the self-consistency of the SGS parameterization with respect to its underlying assumptions. The large-eddy approximation assumes that the energy-containing scales of the flow are resolved by GS motions, while rates of energy dissipation are controlled by SGS processes. Thus, by estimating the relative contribution that SGS processes make to the energy, energy dissipation rates, and fluxes of the simulated flow, the consistency of the SGS models with the large-eddy assumptions may be evaluated. Derivations of the SGS energy and flux levels are given in appendix A.

Initial SGS energy levels range from 7 to 20% of the total KE and PE and dramatically decrease in time to typically less than 5%. The relative contribution GS processes make to the dissipation of KE and PE increases as a function of time although it is generally small (always less than 20% of the total). For the high stratification case (10 cph), less than 4% of the KE dissipation can be attributed to GS processes. In addition, SGS processes make negligible contributions to the domain-averaged buoyancy flux (always less than 1%). Thus, the present LES results are consistent with the assumptions suggested by the large-eddy approximation.

The detailed examination of energy wavenumber spectra provides another means for evaluating the SGS parameterization performance. Horizontal and vertical wavenumber spectra for KE_w and KE_v show noticeable increases in KE levels with wavenumber as the cutoff wavenumber ($k_c = 31$) is approached (Fig. 10). These spectral "roll ups" suggest that transferred KE is not effectively being removed by the Smagorinsky SGS eddy viscosity (Siggia and Patterson 1978). These "roll-ups" are not seen to the same degree in the PE spectra suggesting that PE is being efficiently removed by the SGS parameterization.

Additional information concerning the SGS parameterization may be obtained by examining the spectral variations in the SGS eddy viscosity, K_{SGS}. The spectral distribution of K_{SGS} for the $N = 1$ cph simulation is shown in Fig. 13 at buoyancy times of 1 and 5. Here, the K_{SGS} spectra are given in terms of the spectral variance of the SGS eddy viscosity per individual wave mode. The spectral distributions of K_{SGS} are nearly uniform and isotropic. However, the absolute magnitude of the K_{SGS} spectra are very different for the two times (Fig. 13). Rates of spectral energy transfer due to terms in the equations of motion, which include the SGS eddy viscosity, $\hat{\epsilon}_{sgs}(k_h)$, are also spectrally uniform (Fig. 12). It should be noted that spectral variations in $\hat{\epsilon}_{sgs}(k_v)$ are nearly identical (Siegel 1988) indicating that energy losses due to the SGS parameterization occur isotropically. As was observed in the spectral structure of K_{SGS}, the absolute rates of SGS energy drain decrease with decreasing time, while their spectral shapes remain uniform (Fig. 12).

It has been suggested that a uniform spectral distribution should be found when the Smagorinsky SGS

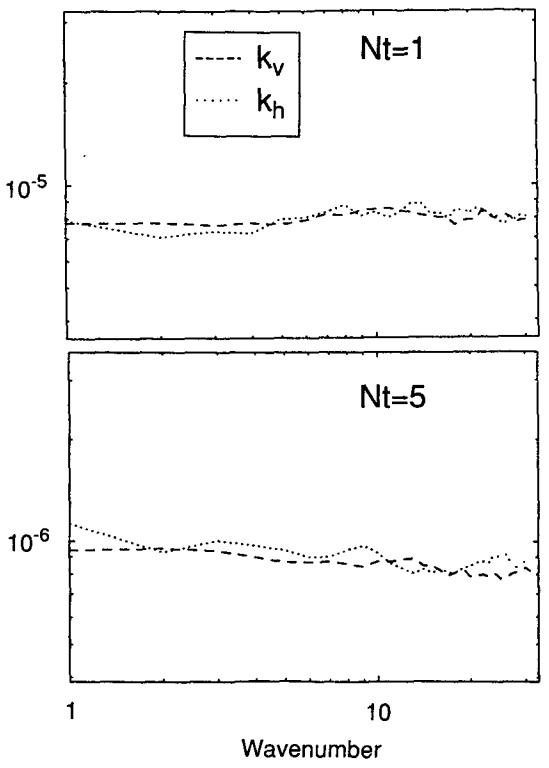

FIG. 13. Horizontal (dotted) and vertical (dashed) wavenumber spectra (per individual wavevector) for the distribution of the Smagorinsky eddy viscosity (K_{SGS}) for the $N = 1$ cph experiment. Buoyancy times (Nt) of 1 and 5 are shown.

eddy viscosity is applied to the large-eddy simulation of isotropic turbulence (e.g., Yoshizawa 1982; Chollet 1984). The fact that holds for the present stably stratified application is somewhat surprising. The uniform and isotropic nature of the spectral distribution of the SGS eddy viscosity suggests that a spatially constant, temporally varying, SGS eddy viscosity may be an appropriate model for the large-eddy simulation of buoyancy-affected flows.

A reasonable candidate SGS parameterization for these purposes is the Chollet and Lesieur (1981, hereafter CL81) spectral SGS eddy viscosity. The CL81 eddy viscosity is constructed by examining spectral energy and scalar variance transfers across a cutoff wavenumber using the Eddy Damped Quasi-Normal Markovian (EDQNM) turbulence model (Chollet and Lesieur 1981; Chollet 1984; Lesieur 1987; Lesieur and Rogallo 1989). The CL81 eddy viscosity accounts for nonlinear energy transfers due to both local and nonlocal triad interactions (e.g., Lesieur 1987). A similar spectral eddy viscosity was derived using the test field model (Kraichnan 1976). The CL81 SGS eddy viscosity has been applied by several investigators to the large-eddy simulation of buoyancy-affected flows (Métais 1985; Lesieur et al. 1988; Siegel 1991; Batchelor et al. 1992; Métais and Lesieur 1992).

The CL81 SGS parameterization is defined by a normalized spectral shape ($K_{\text{norm}}(\mathbf{k}, k_c)$; Fig. 14) whose amplitude is scaled using the kinetic energy at the cutoff wavenumber ($E(k_c)$), or

$$K_{\text{CL81}}(\mathbf{k}, k_c) = \left(\frac{E(k_c)}{k_c}\right)^{1/2} K_{\text{norm}}(\mathbf{k}, k_c)$$

$$= \left(\frac{E(k_c)}{k_c}\right)^{1/2} [0.267 + 9.21 \times \exp(-3.03k_c/|\mathbf{k}|)]. \quad (27)$$

The algorithm for normalized spectra shape, $K_{\text{norm}}(\mathbf{k}, k_c)$, is taken from Lesieur and Rogallo (1989). For low wavenumbers ($|\mathbf{k}|/k_c \ll 1$), the value of $K_{\text{norm}}(\mathbf{k}, k_c)$ is ~ 0.27 while it increases rapidly as it approaches the cutoff wavenumber (Fig. 13). The high wavenumber spectral cusp indicates the importance of local interactions to the transfer of KE across the GS cutoff, whereas the plateau region ($|\mathbf{k}|/k_c \ll 1$) parameterizes the effects of nonlocal interactions (e.g., Lesieur 1987). It should also be noted that spectral eddy viscosities calculated from direct numerical simulations of low Reynolds number isotropic turbulence confirm the existence of a low wavenumber plateau region followed by a high wavenumber cusp (e.g., Domaradzki et al. 1987). Recently, Métais and Lesieur (1992) found a similar result in simulations of stably stratified turbulence.

It is of interest to note that the CL81 amplitude scaling, $(E(k_c)/k_c)^{1/2}$, is reminiscent of Prandtl's mixing length theory where the SGS eddy viscosity scales as the product of a relevant velocity scale and a length scale (e.g., Tennekes and Lumley 1972). For this case, the velocity scale is related to the velocity variance at the cutoff wavenumber $\sqrt{k_c E(k_c)}$ while the length scale is equal to the cutoff scale ($1/k_c$), which is related to the size of an SGS eddy.

A test of the applicability of the CL81 SGS eddy viscosity to the present application would be to examine the degree to which the CL81 amplitude scaling holds for the spectral structure of the Smagorinsky SGS eddy viscosity, K_{SGS}. These wavenumber distributions (Fig. 14) indicate that the Smagorinsky SGS eddy viscosity scales well with $(E(k_c)/k_c)^{1/2}$ with a constant of proportionality of 0.35 (± 0.05). This scaling factor does not appear to differ in either the vertical or horizontal wavenumber directions although the scaling appears to collapse the K_{SGS} variations better in the vertical wavenumber direction than the horizontal. The dif-

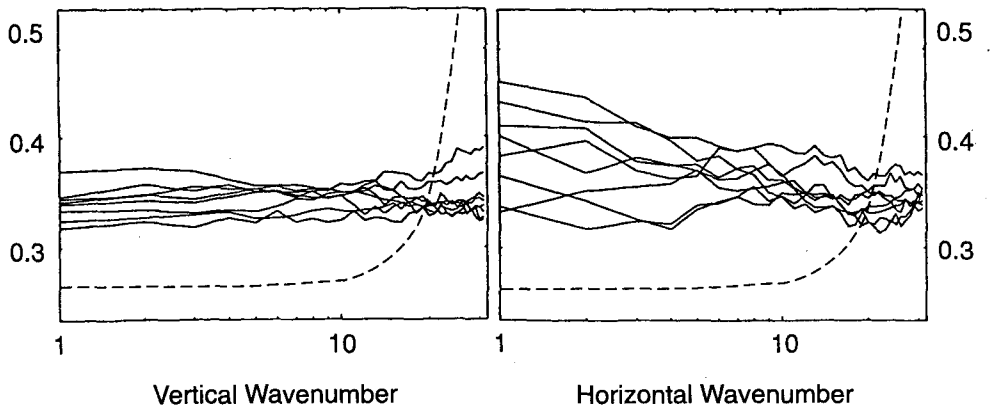

FIG. 14. Spectral variations (per individual wavevector) of the scaled Smagorinsky SGS eddy viscosity $[K_{\text{SGS}}(E(k_c)/k_c)^{-1/2}]$ for the vertical (left panel) and the horizontal (right panel) wavenumbers for the N = 1 cph experiment. The cutoff wavenumber, k_c, is equal to 31. Scaled SGS eddy viscosity spectra are shown for buoyancy times (Nt) of 0.25, 1, 2, 5, 7, and 10.

ference between plateau value of ~0.27 suggested by the CL81 model and the present observation of 0.35 may be attributed to the fact that a high wavenumber cusp is not found in the spectral analysis of the Smagorinsky SGS parameterization. This suggests that the Smagorinsky SGS eddy viscosity compensates for the lack of a high wavenumber cusp by increasing its mean level (Fig. 14). In addition, the high wavenumber "roll ups" observed in the KE spectra (Fig. 10) should be eliminated by introducing an ad hoc high wavenumber augmentation (or cusp) to a constant spectral eddy viscosity (Siggia and Patterson 1978; Siegel 1991).

The present results suggest that the Smagorinsky SGS eddy viscosity may be parameterized as a simple spectral (i.e., uniform and isotropic) function with an amplitude scaling of $(E(k_c)/k_c)^{1/2}$. The CL81 SGS eddy viscosity appears to be a perfect candidate for these purposes. Recently, we have performed several numerical experiments aimed at the evaluation of the CL81 spectral eddy viscosity for stably stratified flows (Siegel 1991). These results indicate that significantly better correspondence is found between observed KE and PE spectra and theoretical Kolmogorov–Obukhov spectra using the CL81 SGS eddy viscosity than were for the Smagorinsky eddy viscosity. In addition, spectral roll ups in KE or PE spectra were not observed. In addition, the CL81 simulations require about one-half the computational time as the Smagorinsky SGS eddy viscosity simulations (Siegel 1991). This work is still in progress.

b. Observations of the turbulent collapse

The "turbulent collapse" refers to the dynamical transition of decaying, 3D, fully developed, stably stratified turbulence to a state where the vertical turbulent scales are suppressed by the ambient stable stratification (e.g., Dickey and Mellor 1980; Stillinger et al. 1983; Gregg 1987; Lesieur 1987; Hopfinger 1987; Barrett and Van Atta 1991). This vertical scale suppression is thought to cause the initially three-dimensional eddies to "collapse" into nearly horizontal "pancakelike" eddies where their vertical scale is limited by the Ozmidov scale (L_0). Observations of these pancake eddies have been made primarily from laboratory flow visualizations of the dispersal of passive dye patches (e.g., Lin and Pao 1979; Browand et al. 1987), while observations of a rapid decrease in energy decay rates or a vanishing buoyancy flux are often used as evidence of the onset of the turbulent collapse (e.g., Dickey and Mellor 1980; Stillinger et al. 1983; Itsweire et al. 1986). Recent laboratory observations have suggested that rates of spectral energy transfer reverse their sign coincident with the onset of the collapse (Itsweire and Helland 1989). Reverse energy transfer cascades are found for the enstrophy cascade in 2D turbulence (Pedlosky 1979). It has been speculated that these "collapsed" eddies are purely 2D vortical motions, creating these reverse energy cascades (e.g., Lilly 1983).

The onset of the turbulent collapse may be best illustrated by making a dimensional argument. We assume that the buoyancy frequency (N), a turbulent vertical velocity scale (w'), and the vertical length scale (h) are the only relevant parameters describing the nature of a decaying, stably stratified, high Reynolds number flow. Using these parameters, a nondimensional group, the Froude number (Fr), may be defined,

$$\mathrm{Fr} = \frac{w'}{Nh} = \frac{\epsilon^{1/3}}{Nh^{2/3}} = \left(\frac{L_0}{h}\right)^{2/3}, \qquad (28)$$

where the turbulent velocity (w') is related to the KE dissipation rate by $\epsilon = w'^3/h$ (Tennekes and Lumley 1972) and the definition of the Ozmidov scale (L_0; 26b) is used. The Froude number quantifies the relative importance of inertial forces (w'^2/h) in the vertical momentum equation to the buoyancy forces (Nw'). For large Fr, the inertial terms (turbulence) should dominate the buoyancy terms (internal waves) in the evolution of vertical momentum. Whereas when Fr is less than one, the buoyancy terms will regulate the evolution of the vertical momentum. As the energy of the flow decays, the relative importance of the inertial forces should diminish, reducing values of Fr. When the Froude number is O(1), the effects of the inertial and buoyancy forces are equal, providing the impetus for the collapse.

The temporal evolution of the Froude number is shown for the three different stratifications in Fig. 15. Initially, values of Fr are much greater than one and decrease monotonically to final values between 0.2 and

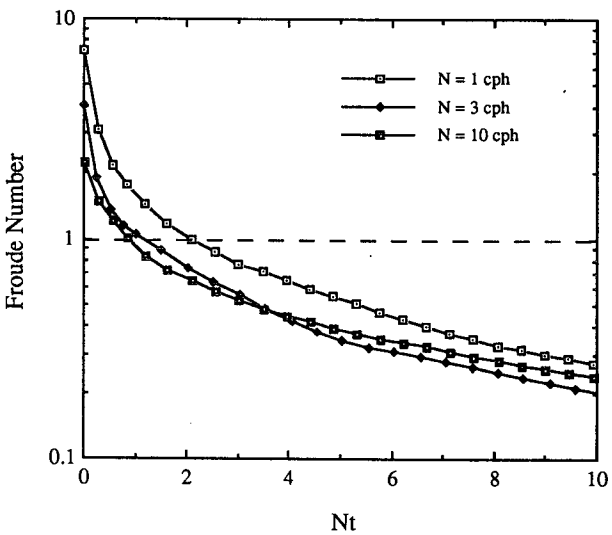

FIG. 15. Temporal evolution of the Froude number [Fr = $(L_0/h)^{2/3}$] for the three mean stratifications. The dashed line corresponds to a Fr of 1. Values of the Froude number greater than one imply that the vertical momentum balance is affected more by inertial forces than by buoyancy forces. For values of Fr less than one, the energy containing scales will be strongly modified by buoyancy forces.

0.3. In general, values of Fr decrease with increasing stratification indicating that buoyancy forces are more important for the higher stratification cases, as is expected. The transition time ($Nt_{tr} \equiv Nt(\mathrm{Fr} = 1)$) is later for the $N = 1$ cph case ($Nt_{tr} \approx 2$) than for the $N = 10$ cph case ($Nt_{tr} \approx 0.8$). These transition times correspond well with the timing of changes observed in the evolution of the buoyancy flux (Fig. 3) where active downgradient turbulent mixing is suppressed after an Nt of ~ 2. For the $N = 10$ cph case, there does not appear to be a clear transition from an irreversible BF to a reversible one, as oscillations in the IBF appear almost immediately (Fig. 3c). This is consistent with the low initial Fr values and the relatively early occurrence of Fr = 1 for the $N = 10$ cph case. Another example of the onset of this turbulent to wavelike transition may be found in the temporal evolution of the vertical–horizontal temperature profile distributions (Fig. 8). However, it is difficult to determine a specific transition time using only these visual data.

The temporal evolution of several domain-averaged quantities appear to give conflicting information about the occurrence of a turbulent collapse. For example, energy decay rates do not decrease coincident with the onset of the collapse (Fig. 1). Further, the size of the vertical integral scale (h) remains unaffected by the onset of the turbulent collapse and roughly the same size of the horizontal energy-containing scale (l; Fig. 6). This result is unexpected as the classical phenomenology predicts that after a turbulent collapse the vertical scale of *turbulent* eddies should decrease in a manner similar to the Ozmidov scale. Thus, we are not seeing a "pancaking" of the energy-containing motions coincident with the collapse. This is especially apparent in the invariance of the energetic structures illustrated in vertical–horizontal cross section view (Fig. 9). However, a dynamic transition does occur in the nature of the BF evolution.

The invariance in the integral length scales indicates that the dynamics of these eddies must have evolved from a fully turbulent state to one in which buoyancy forces are important, although they have retained their size and remain isotropic. In some sense, the constancy of the energy-containing eddies should be expected as it is unlikely that much of the initial low vertical wavenumber VKE would be transferred to higher vertical wavenumbers during a period when the nonlinear transfer mechanisms are inefficient relative to buoyancy processes (when Fr < 1). The low wavenumber VKE would be exchanged with PE, but absolute values of BF are becoming small at this time (Fig. 3). This suggests that the size of the VKE structures should be preserved during the Froude number transition and that the initially turbulent VKE would transform itself into motions where buoyancy processes dominate the dynamics.

The observed lack of "pancaking" may be examined by addressing the evolution of the total vertical energy (TVE), the sum of VKE and PE. A schematic representation of the TVE budget for high Reynolds number stratified turbulence may be expressed as

$$\frac{d\mathrm{TVE}}{dt} = \Phi_V - \epsilon_V - \epsilon_P, \tag{29}$$

where Φ_V is the vertical component of the pressure–strain correlation vector, which represents the exchanges of VKE with HKE and ϵ_V and ϵ_p are the dissipation rates for VKE and PE, respectively. As the buoyancy flux acts only to exchange VKE and PE (21), it does not have any influence upon the evolution of TVE. This suggests that the vertical length scales characteristic of TVE will remain constant during the collapse. Similarly, the nonlinear energy cascades of TVE and, hence, its energy decay rate will remain unaffected by the collapse. Thus, the onset of the collapse only indicates that the evolution of PE and VKE will be intertwined by a reversible BF while energy decay rates, as well as integral length scales, should remain unaffected. These statements will remain true as long as molecular dissipation processes are *not* important for the evolution of the energy-containing motions ($\mathrm{Re}_\lambda \gg 1$).

It should also be noted that reverse KE transfers by nonlinear processes are not observed in any of our LES experiments as is found for the enstrophy cascade of 2D turbulence. Grid-turbulence observations made in a laboratory-based stably stratified water channel suggest that a reversal in the spectral transfer of the downstream energy component in the downstream direction occurs coincidentally with the onset of the turbulent collapse (Itsweire and Helland 1989). The present LES experiments give absolutely no indication of this type of dynamic transition in the KE transfer spectra, not even for $\hat{\Gamma}_{gs}(k_h)$ (Fig. 12). It should be noted that only weak evidence for reverse KE cascades have been observed in 3D stably stratified numerical simulations, and that for an experiment that was specifically designed to observe these effects (Herring and Métais 1989).

The present LES observations show clear evidence of a change in dynamics coincident with the onset of the turbulent collapse. This is primarily observed in the changes of the character of BF as the Froude number becomes less than one (Figs. 3 and 15). However, there exist many differences when compared with most previous laboratory or direct numerical observations of the turbulent collapse. We suggest that this lack of correspondence may be caused by extreme differences in the Reynolds numbers for the flows. For example, Reynolds numbers based upon Taylor length scales (Re_λ) for the present LES results are $O(10^5)$ consistent with typical thermocline values (Siegel 1991). However, Re_λ values observed from laboratory or direct numerical experiments are rarely as large as 70. It should not be expected that these low Re_λ experiments

can realistically simulate the nonlinear interactions found within ocean turbulence as molecular viscous and diffusive processes will have far too important roles in the evolution of the energy-containing motions. Thus, a large-eddy simulation of these flows will provide a very different accounting for these dissipation processes.

Some supporting evidence for our speculation of the role of Reynolds number in the turbulent collapse may be found in Gargett's (1988) scaling analysis. The Gargett scaling applies only at a Froude number of one and hence, only during the onset of the turbulent collapse. Gargett's results state that for high Reynolds number stratified turbulence, the energy-containing length scales and velocity components will remain isotropic (i.e., $h \sim l$ and $u' \sim w'$). Thus, the energetic scales of high Reynolds number stratified turbulence should remain unaffected by the transition to buoyancy-dominated dynamics. However, for low Reynolds number turbulence, the Gargett scaling states that the horizontal length and velocity scales should be greater than respective vertical scales, or $l \geqslant h$ and $u' \geqslant w'$. Thus for a low Reynolds number flow, the effects of the collapse should be apparent in both the length scale and energy level evolution. These predictions are consistent with the present results, although interpretations based upon the Gargett scaling should be made cautiously as several aspects of this analysis have been questioned (Van Atta 1990; Yamazaki 1990).

Recent numerical experiments also provide supporting evidence for a Reynolds number dependency. A low-resolution LES of decaying stably stratified turbulence performed gives results that are consistent with the present observations (Métais 1985). That is, Métais (1985) does not see any evidence of large-scale flow anisotropy forming as a result of the Froude number transition. However, the Métais and Herring (1989) direct numerical simulation does show evidence of a collapse in the evolution of the energy-containing scales. Interestingly, the collapse occurs at nearly the same time as when the Kolmogorov scale grows to roughly the same size at the integral and Ozmidov scales (see Fig. 6 of Métais and Herring 1989). Thus, the energy-containing scales of this direct numerical simulation are affected by molecular processes coincident with the onset of the turbulent collapse and will not satisfy the above arguments concerning the cascading of TVE under high Reynolds number conditions.

There does remain uncertainty concerning the observed lack of "pancaking" of the energetic structures and our ascription of this to the high Reynolds numbers simulated. In particular, there are questions concerning the roles of the SGS parameterization and the initial conditions upon the simulated flow fields. One should note that the evolution of BF (a second-order moment) is predicted consistent with the length scale prediction of the collapse's onset (when Fr $\approx$ 1), whereas the spatial energy distributions (i.e., first-order statistics) are inconsistent with previous low-Re observations of pancaking. It seems odd that the choice of the SGS parameterization, even an isotropic one like the Smagorinsky SGS eddy viscosity, would predict the BF evolution consistent with turbulence phenomenology, but not the flow energetics. Also, the fact that oceanographically relevant vertical eddy diffusivity values are calculated for the latter stages of flow decay suggests that the SGS processes are adequately accounted for. We believe that the reason for this is that the simulated high wavenumber motions perform spectral energy transfers similar to those expected for the inertial subrange of turbulence. Thus, the application of an isotropic SGS eddy viscosity to an evolving stratified flow should be appropriate (see also Métais and Lesieur 1992).

Similarly, it seems unlikely that the initial conditions will have much influence upon the flow's evolution during the collapse. The LES experiments were initialized using a highly anisotropic energy distribution and random phase relations between components. This initial energy distribution evolves rapidly becoming nearly isotropic (in less than $0.25Nt$; Fig. 9). This rapid flow isotropization is caused by the rapid attenuation of high vertical wavenumber energy by SGS dissipation processes as well as GS spectral energy transfers. In a sense, it is this nearly isotropic energy distribution that is really the flow's "initial" condition. We have recently performed LES experiments with isotropic initial energy distributions which confirms many of the present results. In particular, the BF evolution is qualitatively similar. Thus, it is unlikely that the character of the turbulent collapse observed is regulated by the initial conditions.

Therefore, we suggest that the absence of pancaking of the energetic structures is due to the large simulated Reynolds numbers. This suggests that the fundamental nature of decaying stably stratified turbulence is different for oceanographically relevant space and timescales compared with what can be observed using laboratory-based or *direct* numerical techniques. Detailed experiments must be conducted before we can consider the nature of the collapse of stratified turbulence a well understood problem. Some of these questions may be addressed by making additional numerical experiments at differing Reynolds numbers. However, this question might be better addressed by making detailed field measurements of a decaying turbulent feature, such as found in the lee of a tidal channel. It is hoped that the combination of field and numerical methodologies would provide complimentary datasets from which the role of Reynolds number on the decay of turbulence in stably stratified waters might be evaluated.

Acknowledgments. Discussions with Fred Browand, Tom Dickey, Greg Holloway, Jim Riley, and Libe Washburn have been helpful. The detailed comments

by the reviewers, as well as by Libe Washburn, Steven Christie, and Michael Falk, were extremely helpful in revising the manuscript. DAS is presently supported by the Office of Naval Research (N00014-C-09329). JAD was supported during this work by a Research Initiation Grant from the Powell Foundation. Richard Pelz provided the original numerical code from which the present experiments were based. Supercomputer time was provided by a grant from the San Diego Supercomputer Center which is supported by the National Science Foundation.

APPENDIX A

Derivation of the SGS Contribution

SGS energy levels are estimated by assuming that an inertial subrange extends from the GS cutoff wavenumber ($k_c = \pi/\Delta$) to infinity. The assumption of an infinite inertial subrange should lead to a slight overestimate of SGS energy levels. The SGS energy levels are found by integrating the theoretical inertial subrange spectra for KE ($E(k) = \alpha_K \epsilon^{2/3} k^{-5/3}$) and for temperature variance ($E_T(k) = \beta_K \chi \epsilon^{-1/3} k^{-5/3}$) from k_c to infinity. Note, k refers to radial wavenumber,

$$\mathrm{KE}_{\mathrm{sgs}} = \int_{k_c}^{\infty} E(k)dk = 3\alpha_K \left(\frac{\epsilon\Delta}{\pi}\right)^{2/3} \quad \text{(A1a)}$$

$$\mathrm{PE}_{\mathrm{sgs}} = \frac{\alpha^2 g^2}{N^2} \int_{k_c}^{\infty} E_T(k)dk = \frac{3\beta_K \chi \alpha^2 g^2}{2N^2} \left(\frac{\Delta^2}{\epsilon\pi^2}\right)^{1/3}, \quad \text{(A1b)}$$

where α_K is the Kolmogorov constant (~ 1.4) and β_K is the Batchelor constant (~ 1.3; Tennekes and Lumley 1972). These relations enable the SGS energetics to be evaluated as functions of the KE dissipation rate (ϵ) and the temperature variance dissipation rate (χ). The SGS energy relations derived here hold locally as well as in a domain averaged form. The dissipation rates have both GS and SGS components and may be evaluated using the scaling relation (14) or from simplified versions (i.e., excluding buoyancy production) of the KE and temperature variance budgets (e.g., Eidson 1985; Siegel 1988):

$$\epsilon = \epsilon_{\mathrm{gs}} + \epsilon_{\mathrm{sgs}} = \frac{1}{2}\nu \bar{S}^2 + \frac{1}{2} K_{\mathrm{SGS}} \bar{S}^2 \quad \text{(A2a)}$$

$$\chi = \chi_{\mathrm{gs}} + \chi_{\mathrm{sgs}} = \frac{1}{2}\kappa \frac{\partial \bar{T}}{\partial x_i}\frac{\partial \bar{T}}{\partial x_i} + \frac{K_{\mathrm{SGS}}}{2P_{rt}} \frac{\partial \bar{T}}{\partial x_i}\frac{\partial \bar{T}}{\partial x_i}. \quad \text{(A2b)}$$

The potential energy dissipation rate (ϵ_P) is related to the temperature variance dissipation rate (χ) using $\epsilon_P = (\alpha g/N)^2 \chi$. Again, these functions hold over all resolved scales. The GS and SGS contributions to the local buoyancy flux may also be evaluated at any point in space by using the definition of SGS eddy diffusivity (11b), or

$$\mathrm{BF} = \mathrm{BF}_{\mathrm{gs}} + \mathrm{BF}_{\mathrm{sgs}} = g\bar{w}\bar{T} + \frac{g}{\mathrm{Pr}_t} K_{\mathrm{SGS}} \frac{\partial \bar{T}}{\partial x_3}. \quad \text{(A3)}$$

APPENDIX B

Derivation of the Initial Conditions

The initial conditions used in the model are developed based upon a modification of the Garrett–Munk (GM) internal wave spectrum (Munk 1981). The modifications assume that the motions are super inertial (cf. $\omega^2 \gg f^2$) and that the phases of each velocity and buoyancy component are randomly selected (i.e., linear internal wave phase relations are not used). Please note that parameters discussed in this section are in dimensional units. The GM spectrum is built around a nondimensional energy density spectrum often given in terms of a frequency-vertical mode number spectrum ($E_{\mathrm{GM}}(\omega, j)$). The conversion of the $E_{\mathrm{GM}}(\omega, j)$ spectrum (in units of reciprocal frequency and mode number) to $E_{\mathrm{GM}}(k_h, k_v)$ (in units of reciprocal wavenumber squared) is made using the established chain rules of transformation (Garrett and Munk 1972)

$$E_{\mathrm{GM}}(\omega, j)d\omega\delta j = E_{\mathrm{GM}}(k_h, k_v)dk_h dk_v \quad \text{(B1a)}$$

or

$$E_{\mathrm{GM}}(k_h, k_v) = E_{\mathrm{GM}}(\omega, j)\frac{d\omega}{dk_h}\frac{\delta j}{\delta k_v}. \quad \text{(B1b)}$$

The relationship between the frequency and wavenumber is established using the dispersion relation for nonrotating linear internal gravity waves, while the relationship between vertical mode number and wavenumber is made using WKB scaling, or

$$\omega^2 = N^2 \frac{k_h^2}{k_h^2 + k_v^2} = N^2 \cos^2\theta, \quad \text{(B2a)}$$

$$k_v = \frac{\pi j N}{b N_0}, \quad \text{(B2b)}$$

where θ is the angle the wavenumber vector ($\mathbf{k} = (k_h, k_v)$) makes relative to the horizontal, N is the local buoyancy frequency, N_0 is the GM buoyancy frequency scale, and b is the buoyancy frequency scale depth. A tabulation of GM model parameters is found in Table B1. Applying these factors, $E_{\mathrm{GM}}(k_h, k_v)$ is equal to

TABLE B1. GM81 model parameters.

Parameter	Definition	Value
E	energy density	6.3×10^{-3}
b	vertical scale depth	1300 m
j_*	vertical decorrelation mode number	3
$\sum(j^2 + j_*^2)^{-1}$		0.47
N_0	buoyancy frequency scale	3 cph; 5.2×10^{-3} s^{-1}
f	Coriolis parameter (at 30°N)	7.3×10^{-5} s^{-1}

$$E_{GM}(k_h, k_v) = E_{GM}(\omega, j)\frac{Nk_v^2}{(k_h^2 + k_v^2)^{3/2}}\frac{bN_0}{\pi N}. \quad \text{(B3)}$$

The nondimensional energy density for the GM internal wave model ($E_{GM}(\omega, j)$) is given by

$$E_{GM}(\omega, j) = \frac{2Ef}{\pi \sum (j^2 + j_*^2)^{-1}}\frac{1}{\omega(\omega^2 - f^2)^{1/2}}\frac{1}{j^2 + j_*^2}, \quad \text{(B4)}$$

where E is the nondimensional energy density, j_* is the vertical decorrelation mode number, $\sum (j^2 + j_*^2)^{-1}$ represents the infinite sum over the vertical mode number, and f is the Coriolis parameter (at a latitude of 30°N). The $E_{GM}(k_h, k_v)$ spectrum, using the above transformation factors, is equal to

$$E_{GM}(k_h, k_v) = \frac{2EfN_0b}{\sum (j^2 + j_*^2)^{-1}}\frac{k_v^2}{k_h^2}\frac{1}{\sqrt{k_h^2 + k_v^2}}\frac{1}{(k_vN_0b)^2 + (j_*\pi N)^2}. \quad \text{(B5)}$$

Spectra for horizontal velocity, vertical velocity, and temperature may be calculated using the horizontal ($X^2(\omega)$) and vertical ($Z^2(\omega)$) squared displacement functions (Garrett and Munk 1975), or

$$X^2(\omega) = \frac{NN_0b^2}{\omega^4}(\omega^2 + f^2) \quad \text{(B6a)}$$

$$Z^2(\omega) = \frac{N_0b^2}{N\omega^2}(\omega^2 - f^2). \quad \text{(B6b)}$$

The horizontal and vertical velocity spectra may be calculated by multiplying the nondimensional energy density ($E_{GM}(k_h, k_v)$) by $\omega^2X^2(\omega)$ and $\omega^2Z^2(\omega)$, respectively. The temperature spectrum [$F_T(\omega)$] is calculated by multiplying $E_{GM}(k_h, k_v)$ by $(dT_s/dz)^2Z^2(\omega)$. Applying the nonhydrostatic assumption and using the linear dispersion relation to transform ω in terms of k_h and k_v, the dimensional squared horizontal velocity spectrum [$F_u(k_h, k_v)$], the squared vertical velocity spectrum [$F_w(k_h, k_v)$], and the squared temperature spectrum [$F_T(k_h, k_v)$] are given by

$$F_u(k_h, k_v) = NN_0b^2E_{GM}(k_h, k_v) \quad \text{(B7a)}$$

$$F_w(k_h, k_v) = NN_0b^2\frac{k_h^2}{k_h^2 + k_v^2}E_{GM}(k_h, k_v) \quad \text{(B7b)}$$

$$F_T(k_h, k_v) = \frac{N^3N_0b^2}{\alpha^2g^2}E_{GM}(k_h, k_v), \quad \text{(B7c)}$$

where the definition of the buoyancy frequency has been used ($N^2 = \alpha g dT_s/dz$).

The horizontal–vertical wavenumber spectra are converted to vector wavenumber spectra by assuming horizontal isotropy. For the u velocity component, this may be determined using

$$F_u(k_i) = \frac{F_u(k_h, k_v)}{2\pi k_h}, \quad \text{(B8)}$$

where k_i is the 3D wavenumber and $F_u(k_i)$ is the 3D wavenumber distribution of the u-velocity variance.

The initial phases of the wave components are selected randomly from a uniform distribution. Hence, the resulting spectral amplitude and phase of the GS velocity component, $\bar{u}(k_i)$, is equal to

$$\bar{u}(k_i) = (F_u(k_i))^{1/2}(\cos(2\pi r) + i\sin(2\pi r)), \quad \text{(B9)}$$

where r is a random number taken from a uniform distribution. For the $N = 3$ cph experiment, the initial amplitudes were also normally distributed. The effects of this choice on the subsequent evolution of this particular experiment appeared to be minimal (Siegel 1988). After the random velocity fields are created, continuity is imposed by solving a Poisson equation for the pressure field and performing a single time step to correct the initial velocity field (Siegel 1988).

APPENDIX C

Spectral Calculations

Stably stratified flows are axisymmetric as buoyancy forces act to distinguish the vertical component of momentum from the horizontal. Similarly, spatial variations may be different in the vertical direction compared with either of the horizontal directions. However, due to symmetry, stably stratified flows are horizontally isotropic reducing the number of characteristic dimensions from three to two.

Spectral distributions of the flow energetics may be evaluated in the radial, vertical, and horizontal directions. A diagram in spectral space of their relationship to an arbitrary wavevector is shown in Fig. C1. Spectral energy distributions are calculated by accumulating the energy within discrete shells in spectral space. These shells are spherical for radial wavenumbers (k_r), horizontal planes for vertical wavenumbers (k_v), and vertically oriented cylinders for horizontal wavenumbers (k_h) (Fig. C1). For an arbitrary function $\hat{f}(\mathbf{k}; t)$ represented in spectral space, energy spectra may be defined as averages calculated over defined wavenumber shells

$$F_f(k; t) = \sum_{k-\Delta k<|\mathbf{k}|<k+\Delta k} \hat{f}(\mathbf{k}; t)^*\hat{f}(\mathbf{k}; t) = \sum_{k-\Delta k<|\mathbf{k}|<k+\Delta k} \hat{f}(-\mathbf{k}; t)\hat{f}(\mathbf{k}; t), \quad \text{(C1)}$$

where $\Delta k = 1$, k may be defined as k_r ($=(k_x^2 + k_y^2 + k_z^2)^{1/2}$), k_v ($=k_z$), or k_h ($=(k_x^2 + k_y^2)^{1/2}$) (Fig. C1), and the physical space reality condition ($\hat{f}(\mathbf{k}; t)^* = \hat{f}(-\mathbf{k}; t)$) has been applied. Similarly, horizontal–vertical wavenumber spectral energy distributions may be calculated following

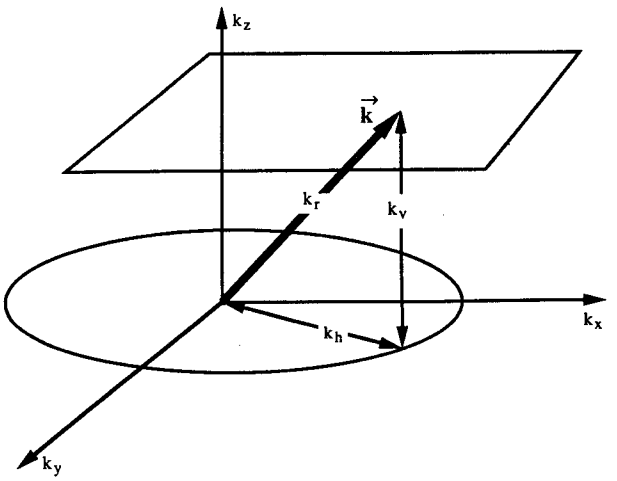

FIG. C1. Diagram of the differences between the spectral wavenumber components used to characterize the flow's spatial structures. The relationship among the radial wavenumber (k_r), the vertical wavenumber (k_v), and the horizontal wavenumber (k_h) are shown in this depiction in spectral space (k_x, k_y, k_z).

$$F_f(k_v, k_h; t) = \sum_{k_v-\Delta k<|\mathbf{k}|<k_v+\Delta k} \sum_{k_h-\Delta k<|\mathbf{k}|<k_h+\Delta k} \hat{f}(-\mathbf{k}; t)\hat{f}(\mathbf{k}; t), \quad \text{(C2)}$$

where spectral averages are effectively calculated over "rings" of spectral space (i.e., the intersection of horizontal planes and vertically oriented cylinders).

It should be noted that the mean energy of a spectral shell is not necessarily the same as the average energy present at each individual wavevector (or mode). Obviously, more wavevectors will fall into a higher radial or horizontal wavenumber shell than in any lower shell. The spectral truncation used to control the effects of aliasing also influences the number of allowable modes per shell. This is particularly important since the higher wavenumber shells often contain wavenumber modes that have been eliminated by the dealiasing procedure. The number of modes per shell for one-dimensional radial, vertical, and horizontal spectra is shown in Fig. C2. A similar depiction for the two-dimensional wavenumber spectra is shown in Fig. C3. The number of modes per wavenumber shell enable the energy for each wavenumber shell and each wavevector, or mode, to be calculated interchangeably.

As described in the text, wavenumbers are given in integer values and the domain size is 10 m. This means that a wavenumber of one corresponds to a dimensional spatial scale of 10 m and a wavenumber of 10 corresponds to a spatial scale of 1 m. The integer wavenumber of the smallest resolved scale is 31, which corresponds to spatial scale of 0.323 m.

APPENDIX D

Calculating Rates of Spectral Energy Transfer

The contributions of various dynamical processes to the energetics of the flow may be evaluated as a function of scale by evaluating the spectral energy transfer budget. The energy transfer budget may be derived by first expressing the equations of motion in spectral space (e.g., Schumann and Patterson 1978b; Lesieur 1987), or

$$\frac{\partial \hat{u}_i}{\partial t} + \nu k^2 \hat{u}_i = \hat{\tau}_{gsi} + \hat{\tau}_{sgsi} - ik_i\hat{p} + g\delta_{i3}\hat{T} \quad \text{(D1a)}$$

$$\frac{\partial \hat{T}}{\partial t} + \kappa k^2 \hat{T} = \hat{\eta}_{gs} + \hat{\eta}_{sgs} - \hat{u}_3 \frac{dT_s}{dx_3} \quad \text{(D1b)}$$

$$k_i \hat{u}_i = 0, \quad \text{(D1c)}$$

where $\hat{u}_i$ is the velocity field represented in spectral space (a function of the vector wavenumber, $\mathbf{k}$ or k_i, and time); $\hat{T}$ is the temperature fluctuation spectrum; the terms $\hat{\tau}_{gsi}$ and $\hat{\tau}_{sgsi}$ ($\hat{\eta}_{gs}$ and $\hat{\eta}_{sgs}$) represent the grid-scale nonlinear and parameterized subgrid-scale flux terms in the momentum (temperature fluctuation) expressions [Eq. (12)] and i is the imaginary number. The GS nonlinear and SGS flux terms may be defined in spectral space as

$$\hat{\tau}_{gsi} = (\epsilon_{ijk}\widehat{\bar{u}_j\bar{\Omega}_k}) - \left(\frac{\partial(\widehat{\bar{u}_j\bar{u}_j})/2}{\partial x_i}\right) \quad \text{(D2a)}$$

$$\hat{\tau}_{sgsi} = \left(\frac{\partial \widehat{K\bar{S}_{ij}}}{\partial x_j}\right) - \left(\frac{\partial(\widehat{\overline{u_j'u_j'}})/2}{\partial x_i}\right) \quad \text{(D2b)}$$

$$\hat{\eta}_{gs} = \left(-\frac{\partial \widehat{\bar{u}_j\bar{T}}}{\partial x_j}\right) \quad \text{(D2c)}$$

$$\hat{\eta}_{sgs} = \left(\frac{1}{\mathrm{Pr}_t}\frac{\partial}{\partial x_j}\widehat{K\frac{\partial \bar{T}}{\partial x_j}}\right), \quad \text{(D2d)}$$

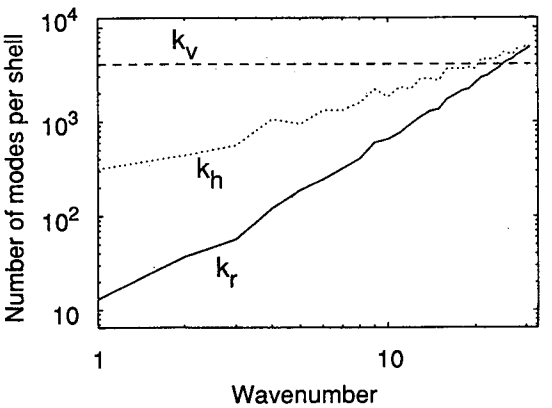

FIG. C2. Spectral distribution of the number of modes in each 1D shell average. Distributions are shown for the radial wavenumber (k_r: solid), the horizontal wavenumber (k_r: dotted), and the vertical wavenumber (k_r: dotted).

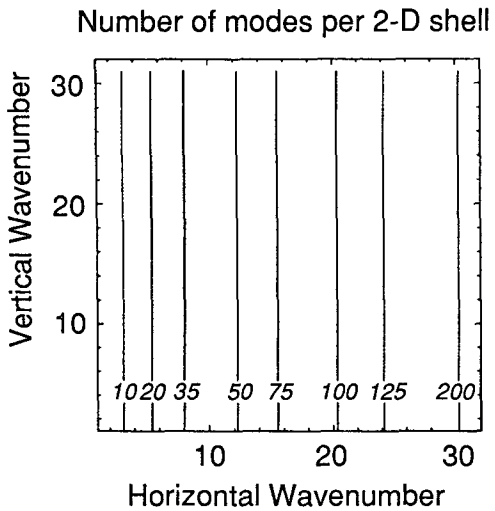

FIG. C3. Spectral distribution (in $k_h - k_v$ space) of the number of modes in each horizontal–vertical wavenumber shell average. The number of modes per shell increases from left to right. The indicated levels are 10, 20, 35, 50, 75, 100, 125, and 200.

where the brackets with the caret on top corresponds to the term inside the bracket represented in spectral space. Spectral energy expressions are derived by multiplying the ith component of the momentum equation by the complex conjugate of the jth velocity component [$\hat{u}_j(\mathbf{k})^* = \hat{u}_j(-\mathbf{k})$] and multiplying the temperature equation by $(g^2/2)\hat{T}(\mathbf{k})^*$. The indices in the momentum equation are switched (i.e., the jth equation is dotted with ith velocity component) and the two equations are summed together. The resulting spectral energy equations may be written as

$$\frac{\partial \hat{E}_{ij}}{\partial t} + \hat{\epsilon}_{ij} = \hat{\Gamma}_{gsij} + \hat{\Gamma}_{sgsij} + \hat{\Phi}_{ij} + \hat{B}_{ij} \quad \text{(D3a)}$$

$$\frac{\partial \hat{P}}{\partial t} + \hat{\chi} = \hat{\Psi}_{gs} + \hat{\Psi}_{sgs} - \hat{B}_{33}, \quad \text{(D3b)}$$

where $\hat{E}_{ij}$ are the component kinetic energy (for $i = j$; not summed) and Reynolds stress (for $i \neq j$) spectra, and $\hat{P}$ is the potential energy spectrum,

$$\hat{E}_{ij}(\mathbf{k}) = \frac{1}{2}\hat{u}_i(\mathbf{k})\hat{u}_j(-\mathbf{k}) \quad \text{(D4a)}$$

$$\hat{P}(\mathbf{k}) = \frac{g^2}{2}\hat{T}(\mathbf{k})\hat{T}(-\mathbf{k}). \quad \text{(D4b)}$$

Here $\hat{\Gamma}_{gsij}$ and $\hat{\Gamma}_{sgsij}(\hat{\Psi}_{gs} + \hat{\Psi}_{sgs})$ represent the nonlinear kinetic (potential) energy transfer due to the GS and SGS processes, respectively, or

$$\hat{\Gamma}_{gsij}(\mathbf{k}) = \frac{1}{2}(\hat{\tau}_{gsi}(\mathbf{k})\hat{u}_j(-\mathbf{k}) + \hat{\tau}_{gsj}(\mathbf{k})\hat{u}_i(-\mathbf{k})) \quad \text{(D4c)}$$

$$\hat{\Gamma}_{sgsij}(\mathbf{k}) = \frac{1}{2}(\hat{\tau}_{sgsi}(\mathbf{k})\hat{u}_j(-\mathbf{k}) + \hat{\tau}_{sgsj}(\mathbf{k})\hat{u}_i(-\mathbf{k})) \quad \text{(D4d)}$$

$$\hat{\Psi}_{gs}(\mathbf{k}) = \frac{g^2}{2}\hat{\eta}_{gs}(\mathbf{k})\hat{T}(-\mathbf{k}) \quad \text{(D4e)}$$

$$\hat{\Psi}_{sgs}(\mathbf{k}) = \frac{g^2}{2}\hat{\eta}_{sgs}(\mathbf{k})\hat{T}(-\mathbf{k}); \quad \text{(D4f)}$$

$\hat{\Phi}_{ij}$ is the pressure–strain correlation spectrum,

$$\hat{\Phi}_{ij}(\mathbf{k}) = \frac{-i}{2}\hat{p}(\mathbf{k})(k_i\hat{u}_j(-\mathbf{k}) + k_j\hat{u}_i(-\mathbf{k})); \quad \text{(D4g)}$$

$\hat{B}_{ij}$ is the buoyancy flux spectrum,

$$\hat{B}_{ij}(\mathbf{k}) = \frac{g^2}{2}\hat{T}(\mathbf{k})(\delta_{i3}\hat{u}_j(-\mathbf{k}) + \delta_{j3}\hat{u}_i(-\mathbf{k})); \quad \text{(D4h)}$$

and $\hat{\epsilon}_{ij}$ and $\hat{\chi}$ represent the energy losses due to molecular viscous and diffusive processes and are given

$$\hat{\epsilon}_{ij}(\mathbf{k}) = 2\nu k^2 \hat{E}_{ij}(\mathbf{k}) \quad \text{(D4i)}$$

$$\hat{\chi}(\mathbf{k}) = 2\kappa k^2 \hat{P}(\mathbf{k}). \quad \text{(D4j)}$$

In general, rates of energy transfer due to molecular processes will be negligibly small due the high Reynolds numbers simulated (Siegel 1988).

These expressions may be used to evaluate the effects of the different dynamical processes upon the evolution of the energy spectra using the LES data fields. The terms comprising the spectral transfer of horizontal kinetic energy [HKE; $\hat{E}_{11}(\mathbf{k}) + \hat{E}_{22}(\mathbf{k})$] are evaluated separately from the vertical kinetic energy spectral transfer terms [VKE; $\hat{E}_{33}(\mathbf{k})$] because of the axisymmetric nature of stably stratified flows.

REFERENCES

Barrett, T. K., and C. W. Van Atta, 1991: Experiments on the inhibition of mixing in stably stratified decaying turbulence using laser Doppler anemometry and laser-induced fluorescence. *Phys. Fluids A*, **3**, 1321–1332.

Batchelor, G. K., V. M. Canuto, and J. R. Chasnov, 1992: Homogeneous buoyancy-generated turbulence. *J. Fluid Mech.*, **235**, 349–378.

Browand, F. K., D. Guyomar, and S.-C. Yoon, 1987: The behavior of a turbulent front in a stratified fluid: Experiments with an oscillating grid. *J. Geophys. Res.*, **92**, 5329–5341.

Caldwell, D. R., 1983: Oceanic turbulence: Big bangs or continuous creation? *J. Geophys. Res.*, **88**, 7543–7550.

Canuto, C., M. Y. Hussaini, A. Quarteroni, and T. A. Zang, 1988: *Spectral Methods in Fluid Dynamics*. Springer-Verlag, 567 pp.

Chollet, J. P., 1984: Two point closures as a subgrid scale modeling for large eddy simulations. *Turbulent Shear Flows IV*, F. Durst and B. Launder, Eds., Springer-Verlag, 62–72.

——, and M. Lesieur, 1981: Parameterization of small scales of three-dimensional isotropic turbulence utilizing spectral closures. *J. Atmos. Sci.*, **38**, 2747–2757.

Clark, R. A., J. H. Ferziger, and W. C. Reynolds, 1979: Evaluation of subgrid-scale turbulence models using a fully simulated turbulent flow. *J. Fluid Mech.*, **91**, 1–16.

Crawford, W. R., 1986: A comparison of length scales and decay times of turbulence in stably stratified flows. *J. Phys. Oceanogr.*, **16**, 1847–1854.

Deardorff, J. W., 1970: A numerical study of three-dimensional turbulent channel flow at large Reynolds numbers. *J. Fluid Mech.*, **41**, 453–480.

——, 1973: Three-dimensional numerical modeling of the planetary boundary layer. *Workshop on Micrometeorology,* D. Haugen, Ed., Amer. Meteor. Soc., 271–311.
——, 1974: Three-dimensional numerical study of the height and mean structure of a heated planetary boundary layer. *Bound.-Layer Meteor.,* **7,** 81–106.
——, 1980: Stratocumulus-capped mixed layer derived from a three-dimensional model. *Bound.-Layer Meteor.,* **18,** 495–527.
Dickey, T. D., and G. L. Mellor, 1980: Decaying turbulence in neutral and stratified fluids. *J. Fluid Mech.,* **99,** 13–31.
Dillon, T. M., 1982: Vertical overturns: A comparison of Thorpe and Ozmidov scales. *J. Geophys. Res.,* **87,** 9601–9613.
——, 1984: The energetics of overturning structures: Implications for the theory of fossil turbulence. *J. Phys. Oceanogr.,* **14,** 541–549.
Domaradzki, J. A., and G. L. Mellor, 1984: A simple turbulence closure hypothesis for the triple-velocity correlation functions in homogeneous isotropic turbulence. *J. Fluid Mech.,* **140,** 45–61.
——, R. W. Metcalfe, R. S. Rogallo, and J. J. Riley, 1987: Analysis of subgrid-scale eddy viscosity with use of results from direct numerical simulations. *Phys. Rev. Lett.,* **58,** 547–550.
Ebert, E. E., U. Schumann, and R. B. Stull, 1989: Nonlocal turbulent mixing in the convective boundary layer evaluated from a large-eddy simulation. *J. Atmos. Sci.,* **46,** 2178–2207.
Eidson, T. M., 1982: Numerical simulation of the turbulent Rayleigh–Bénard problem using subgrid modelling. Ph.D. dissertation, University of Michigan, 177 pp.
——, 1985: Numerical simulation of the turbulent Rayleigh–Bénard problem using subgrid modelling. *J. Fluid Mech.,* **158,** 245–268.
Ferziger, J. H., 1983: Higher-level simulations of turbulent flows. *Computational Methods for Turbulent, Transonic, and Viscous Flows.* J. A. Essers, Ed., Hemisphere, 93–182.
Gallacher, P. C., 1990: Large-eddy simulations of the turbulent boundary layer in the upper ocean (abstract only). *Eos, Trans. Amer. Geophys. Union,* **71,** 1354.
Gargett, A. E., 1984: Vertical eddy diffusivity in the oceanic interior. *J. Mar. Res.,* **42,** 359–393.
——, 1988: The scaling of turbulence in the presence of stable stratification. *J. Geophys. Res.,* **93,** 5021–5036.
——, P. J. Hendricks, T. B. Sanford, T. R. Osborn, and A. J. Williams III, 1981: A composite spectrum of vertical shear in the upper ocean. *J. Phys. Oceanogr.,* **11,** 1258–1271.
——, T. R. Osborn, and P. W. Nasmyth, 1984: Local isotropy and the decay of turbulence in a stratified fluid. *J. Fluid Mech.,* **144,** 231–280.
Garrett, C., and W. Munk, 1972: Space-time scales of internal waves. *Geophys. Fluid Dyn.,* **2,** 225–264.
——, and ——, 1975: Space-time scales of internal waves: A progress report. *J. Geophys. Res.,* **80,** 291–297; Corrigendum. *J. Geophys. Res.,* **80,** 3924.
Gibson, C. H., 1980: Fossil temperature, salinity and vorticity turbulence in the ocean. *Marine Turbulence,* J. C. J. Nihoul, Ed., Elsevier, 221–257.
——, 1987: Fossil turbulence and intermittency in sampling oceanic mixing processes. *J. Geophys. Res.,* **92,** 5383–5404.
Gregg, M. C., 1977: Comparing fine structure spectra from the main thermocline. *J. Phys. Oceanogr.,* **7,** 33–40.
——, 1987: Diapycnal mixing in the thermocline: A review. *J. Geophys. Res.,* **92,** 5249–5286.
——, 1989: Scaling turbulent dissipation in the thermocline. *J. Geophys. Res.,* **94,** 9686–9698.
——, 1991: The study of mixing in the ocean: A brief history. *Oceanography,* **4,** 39–45.
——, and T. B. Sanford, 1988: The dependence of turbulent dissipation on stratification in a diffusively stable thermocline. *J. Geophys. Res.,* **93,** 12 381–12 392.
——, E. A. D'Asaro, T. J. Shay, and N. Larson, 1986: Observations of persistent mixing and near-inertial waves internal waves. *J. Phys. Oceanogr.,* **16,** 856–885.
——, D. P. Winkel, T. B. Sanford, 1993: Varieties of fully resolved spectra of vertical shear. *J. Phys. Oceanogr.,* **23,** 124–141.
Grötzbach, G., 1980: Numerical simulation of turbulent temperature fluctuations in liquid metals. *Int. J. Heat Mass Trans.,* **24,** 475–490.
——, and U. Schumann, 1979: Direct numerical simulation of turbulent velocity, pressure, and temperature fields in channel flows. *Turbulent Shear Flows I,* F. Durst, B. Launder, F. Schmidt, and J. Whitelaw, Eds., Springer-Verlag, 370–385.
Hebert, D., J. N. Moum, C. A. Paulson, D. R. Caldwell, 1992: Turbulence and internal waves at the equator. Part II: Details of a single event. *J. Phys. Oceanogr.,* **22,** 1346–1356.
Henyey, F. S., J. Wright, and S. M. Flatté, 1986: Energy and action flow through the internal wave field: An Eikonal approach. *J. Geophys. Res.,* **91,** 8487–8495.
Herring, J. R., and J. C. McWilliams, 1985: Comparison of direct numerical simulation of two-dimensional turbulence with two-point closure: The effects of intermittency. *J. Fluid Mech.,* **153,** 229–242.
——, and O. Métais, 1989: Numerical experiments in forced stably stratified turbulence. *J. Fluid Mech.,* **202,** 97–115.
——, S. A. Orszag, R. H. Kraichnan, and D. G. Fox, 1974: Decay of two-dimensional homogeneous turbulence. *J. Fluid Mech.,* **66,** 5417–5444.
Holland, W. R., and L. B. Lin, 1975: On the origin of mesoscale eddies and their contribution to the general circulation of the ocean. I. A preliminary numerical experiment. *J. Phys. Oceanogr.,* **5,** 642–657.
Holloway, G., 1983: A conjecture relating oceanic internal waves and small-scale processes. *Atmos.-Ocean,* **21,** 107–122.
——, 1988: The buoyancy flux from internal gravity wave breaking. *Dyn. Atmos. Oceans,* **12,** 107–125.
——, and D. Ramsden, 1988: Theories of internal wave interaction and stably-stratified turbulence: Testing against direct numerical experimentation. *Small-Scale Turbulence and Mixing in the Ocean,* J. C. J. Nihoul and B. M. Jamart, Eds., Elsevier, 363–377.
Hopfinger, E. J., 1987: Turbulence in stratified fluids: A review. *J. Geophys. Res.,* **92,** 5287–5303.
Itsweire, E. C., and K. N. Helland, 1989: Spectra and energy transfer in stably stratified turbulence. *J. Fluid Mech.,* **207,** 419–452.
——, ——, and C. W. Van Atta, 1986: The evolution of grid-generated turbulence in a stably stratified fluid. *J. Fluid Mech.,* **162,** 299–338.
Kerr, R. M., 1990: Velocity, scalar and transfer spectra in numerical turbulence. *J. Fluid Mech.,* **211,** 309–332.
Kraichnan, R. H., 1976: Eddy viscosity in two and three dimensions. *J. Atmos. Sci.,* **33,** 1521–1536.
Kunze, E., M. G. Briscoe, and A. J. Williams III, 1990: Interpreting shear and strain fine structure from a neutrally buoyant float. *J. Geophys. Res.,* **95,** 18 111–18 125.
Kwak, D., 1975: Three-dimensional time dependent computation of turbulent flow. Ph.D. dissertation, Stanford University, 124 pp.
Lelong, P., and J. J. Riley, 1992: Weakly nonlinear wave/vortical mode interactions in strongly-stratified flows. *J. Fluid Mech.,* **232,** 1–19.
Leonard, A., 1974: Energy cascades in large eddy simulations of turbulent fluid flows. *Advances in Geophysics,* Vol. 18, Academic Press, 237–248.
Lesieur, M., 1987: *Turbulence in Fluids.* Martius Nijhoff, 286 pp.
——, and R. Rogallo, 1989: Large-eddy simulation of passive scalar diffusion in isotropic turbulence. *Phys. Fluids A,* **1,** 718–722.
——, O. Métais, and H. Laroche, 1988: Numerical simulations of turbulent stably-stratified and free shear flows. *Extended Abstract, Eighth Symp. on Turbulence and Diffusion,* Amer. Meteor. Soc., 57–60.
Lienhard, J. H. V., and C. W. Van Atta, 1990: The decay of thermally stratified turbulence. *J. Fluid Mech.,* **210,** 57–112.

Lilly, D. K., 1983: Stratified turbulence and the mesoscale variability of the atmosphere. *J. Atmos. Sci.*, **40,** 749–761.

——, 1989: Subgrid scale closures in large-eddy simulations. *Lecture Notes on Turbulence,* J. Herring and J. McWilliams, Eds., World Scientific, 207–218.

Lin, J. T., and Y. H. Pao, 1979: Wakes in stratified fluids. *Annu. Rev. Fluid Mech.*, **11,** 317–338.

Mansour, N. N., P. Moin, W. C. Reynolds, and J. H. Ferziger, 1979: Improved methods for large eddy simulations of turbulence. *Turbulent Shear Flows I,* F. Durst, B. Launder, F. Schmidt, and J. Whitelaw, Eds., Springer-Verlag, 386–401.

Mason, P. J., 1989: Large-eddy simulation of the convective atmospheric boundary layer. *J. Atmos. Sci.*, **46,** 1492–1516.

——, and S. H. Derbyshire, 1990: Large-eddy simulation of the stably-stratified atmospheric boundary layer. *Bound.-Layer Meteor.*, **53,** 117–162.

McEwan, A. D., 1983: Internal mixing in stratified fluids. *J. Fluid Mech.*, **128,** 59–80.

McWilliams, J. C., P. C. Gallacher, C.-H. Moeng, and J. Wyngaard, 1993: Large-eddy simulations of oceanic boundary layers. *Large Eddy Simulations,* B. Galperin and S. Orszag, Eds., Cambridge Press, 441–454.

Métais, O., 1985: Evolution of three dimensional turbulence under stratification. *Turbulence in Fluids,* Mantius Nijhoff, 245–248.

——, and J. R. Herring, 1989: Numerical simulations of freely evolving turbulence in stably stratified fluids. *J. Fluid Mech.*, **202,** 117–148.

——, and M. Lesieur, 1992: Spectral large-eddy simulation of isotropic and stably stratified turbulence. *J. Fluid Mech.*, **202,** 117–148.

Moeng, C.-H., 1984: A large-eddy simulation model for the study of planetary boundary-layer turbulence. *J. Atmos. Sci.*, **41,** 2052–2062.

——, and J. C. Wyngaard, 1988: Spectral analysis of large-eddy simulations of the convective boundary-layer. *J. Atmos. Sci.*, **45,** 3573–3587.

Monin, A. S., and A. M. Yaglom, 1981: *Statistical Fluid Mechanics: Mechanics of Turbulence.* Vol. 2. J. Lumley, Ed., The MIT Press, 874 pp.

Moum, J. N., 1990: The quest for $K\rho$—preliminary results from direct measurement of turbulent fluxes in the ocean. *J. Phys. Oceanogr.*, **20,** 1980–1984.

Müller, P., 1984: Small-scale vortical motions. *Internal Gravity Waves and Small-Scale Turbulence, Proc. 'Aha Huliko'a Hawaiian Winter Workshop,* Hawaii Institute of Geophysics, 300 pp.

——, 1988: Vortical motions. *Small-Scale Turbulence and Mixing in the Ocean,* J. C. J. Nihoul and B. M. Jamart, Eds., Elsevier, 285–301.

——, D. J. Olbers, and J. Willebrand, 1978: The IWEX spectrum. *J. Geophys. Res.*, **83,** 479–500.

——, G. Holloway, F. Henyey, and N. Pomphrey, 1986: Nonlinear interactions among internal gravity waves. *Rev. Geophys.*, **24,** 493–536.

Munk, W. H., 1966: Abyssal recipes. *Deep-Sea Res.*, **13,** 707–730.

——, 1981: Internal waves and small-scale processes. *Evolution of Physical Oceanography,* B. Warren and C. Wunsch, Eds., The MIT Press, 264–291.

Oakey, N. S., 1982: Determination of the rate of dissipation of turbulent energy from simultaneous temperature and velocity shear microstructure measurements. *J. Phys. Oceanogr.*, **12,** 256–271.

Onken, R., 1992: Mesoscale upwelling and density finestructure in the seasonal thermocline—a dynamical model. *J. Phys. Oceanogr.*, **22,** 1257–1273.

Orlanski, I., and C. P. Cerasoli, 1981: Energy transfer among internal gravity modes: Weak and strong interactions. *J. Geophys. Res.*, **85,** 4103–4124.

Orszag, S., 1971a: Numerical simulation of incompressible flows within simple boundaries. I. Galerkin (spectral) representations. *Stud. Appl. Math.*, **50,** 293–327.

——, 1971b: Numerical simulation of incompressible flows within simple boundaries: Accuracy. *J. Fluid Mech.*, **49,** 75–112.

——, and G. S. Patterson, 1972: Numerical simulation of three-dimensional homogeneous isotropic turbulence. *Phys. Rev. Lett.*, **28,** 76–79.

Osborn, T. R., 1980: Estimates of the local rate of vertical diffusion from dissipation measurements. *J. Phys. Oceanogr.*, **10,** 83–89.

——, and C. S. Cox, 1972: Oceanic fine structure. *Geophys. Fluid Dyn.*, **3,** 321–345.

Pedlosky, J., 1979: *Geophysical Fluid Dynamics.* Academic Press, 624 pp.

Phillips, O. M., 1980: *The Dynamics of the Upper Ocean.* Cambridge University Press, 336 pp.

Pinkel, R., 1984: Doppler sonar observations of internal waves: The wavenumber frequency spectrum. *J. Phys. Oceanogr.*, **14,** 1249–1270.

——, J. T. Sherman, J. A. Smith, and S. Anderson, 1991: Strain: Observations of the vertical gradient of isopycnal vertical displacement. *J. Phys. Oceanogr.*, **21,** 527–540.

Piomelli, U., P. Moin, and J. H. Ferziger, 1989: Model consistency in large-eddy simulation of turbulent channel flows. *Phys. Fluids,* **31,** 1884–1891.

Ramsden, D., and G. Holloway, 1991: Energy transfers across an internal wave vortical model spectrum. *J. Geophys. Res.*, **97,** 3659–3668.

Riley, J. J., R. W. Metcalfe, and M. A. Weissman, 1981: Direct numerical simulations of homogeneous turbulence in density-stratified fluids. *AIP Conf. Nonlinear Properties of Internal Waves,* La Jolla, CA, AIP, 79–112.

Rogallo, R., and P. Moin, 1984: Numerical simulations of turbulent flows. *Annu. Rev. Fluid Mech.*, **16,** 99–137.

Schmidt, H., and U. Schumann, 1989: Coherent structure of the convective boundary layer derived from large-eddy simulations. *J. Fluid Mech.*, **200,** 511–562.

Schumann, U., 1975: Subgrid-scale model for finite difference simulations of turbulent shear flows in plane channels and annuli. *J. Comput. Phys.*, **18,** 376–404.

——, 1991: Subgrid length-scales for large-eddy simulation of stratified turbulence. *Theoretical and Computational Fluid Dynamics,* T. Gatski and C. Speziale, Eds., Springer-Verlag, 15 pp.

——, and G. S. Patterson, 1978a: Numerical study of pressure and velocity fluctuations in nearly isotropic turbulence. *J. Fluid Mech.*, **88,** 685–709.

——, and ——, 1978b: Numerical study of the return of axisymmetric turbulence to isotropy. *J. Fluid Mech.*, **88,** 711–735.

Shen, C. Y., and G. Holloway, 1986: A numerical study of the frequency and the energetics of nonlinear internal gravity waves. *J. Geophys. Res.*, **91,** 953–973.

Siegel, D. A., 1988: Large-eddy simulation of the decay of a small-scale oceanic internal gravity wave field. Ph.D. dissertation, University of Southern California, 187 pp.

——, 1991: Large-eddy simulation of internal wave motions. *Proc. 'Aha Huliko'a Winter Workshop on Internal Gravity Wave Dynamics,* Hawaii Institute of Geophysics, 135–155.

Siggia, E. D., and G. S. Patterson, 1978: Intermittency effects in a numerical simulation of stationary three-dimensional turbulence. *J. Fluid Mech.*, **86,** 567–592.

Smagorinsky, J., 1963: General circulation experiments with the primitive equations. *Mon. Wea. Rev.*, **91,** 99–164.

Stewart, R. W., 1969: Turbulence and waves in a stratified atmosphere. *Radio Sci.*, **4,** 1269–1278.

Stillinger, D. C., K. N. Helland, and C. W. Van Atta, 1983: Experiments on the transition of homogeneous turbulence to internal waves in a stratified fluid. *J. Fluid Mech.*, **131,** 91–122.

Tennekes, H., and J. L. Lumley, 1972: *A First Course in Turbulence.* The MIT Press, 300 pp.

Thorpe, S. A., 1977: Turbulence and mixing in a Scottish loch. *Proc. Roy. Soc. London,* **A286,** 125–181.

Van Atta, C., 1990: Comment on "The scaling of turbulence in the presence of stable stratification" by A. E. Gargett. *J. Geophys. Res.,* **95,** 11 673–11 674.

Weissman, M. A., R. W. Metcalfe, and J. J. Riley, 1981: Non-linear internal wave interactions. *AIP Conf. Nonlinear Properties of Internal Waves,* La Jolla, CA, AIP, 253–266.

Winters, K. B., and E. A. D'Asaro, 1989: Two-dimensional instability of finite amplitude internal gravity wave packets near a critical level. *J. Geophys. Res.,* **94,** 12 709–12 719.

——, and J. J. Riley, 1992: Instability of internal waves near a critical level. *Dyn. Atmos. Oceans,* **16,** 249–278.

Yamazaki, H., 1990: Stratified turbulence near a critical dissipation rate. *J. Phys. Oceanogr.,* **20,** 1583–1598.

Yoshizawa, A., 1982: A statistically derived subgrid scale model for large eddy simulation of turbulence. *Phys. Fluids,* **25,** 1532–1538.